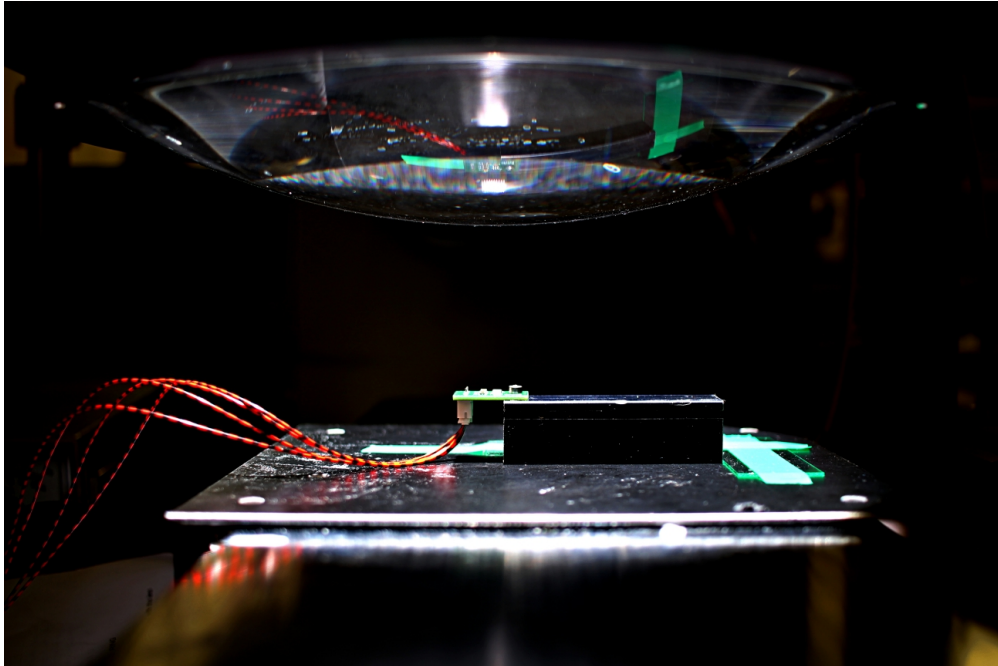


Outdoor solar cell performance

Improving a diffuseness measurement tool



student merlijn Kersten (AUC, kerstenmerlijn@gmail.com)
supervisors dr. Forrest Bradbury (AUC, f.r.bradbury@auc.nl)
dr. Bruno Ehrler (AMOLF, b.ehrler@amolf.nl)
reader dr. Esther Alarcón Lladó (AMOLF, e.alarconllado@amolf.nl)
tutor dr. Cor Zonneveld (AUC, c.zonneveld@auc.nl)

date Wednesday, 30 May 2018
major science
word count 9257

keywords solar cells, outdoor performance, diffuse light,
modelling, sensor characterisation

Abstract

In order to restrict global warming to levels below those agreed upon in the Paris climate agreement, the emission of greenhouse gasses has to be reduced drastically. This can be done by increasing the share of renewable energy sources in energy production. Solar energy has a large growth potential and it is therefore important to study the outdoor performance of solar cells so that one can make informed decisions about their implementation. In order to do this, we need instruments that can measure outdoor conditions important to solar energy. This report is concerned with improving an instrument that measures the diffuseness of incoming solar light, which can then be used to study the affect of diffuse lighting conditions on solar panels. With rise in use of bifacial panels, diffuse lighting is increasingly important.

This thesis was written as part of an internship at AMOLF, which has developed a cubical diffuseness measurement tool. Through a simulation, we found that this tool could be improved by increasing the number of sensors from six to twelve. This would greatly increase the accuracy of the instrument, even when taking into account error introduced by shading of sensors by parts of the instrument.

At the moment, the AMOLF workshop is building a prototype of the instrument. By characterising some of the sensors that will be used on this prototype, we found that only limited calibration of the offset of new sensors is needed to obtain reliable measurements. When the prototype is completed, the results of this report will be experimentally tested at the solar array outside of the AMOLF office.

Front image: A sensor illuminated by the solar simulator.

Preface

Presented before you is my bachelor thesis, which I wrote during my capstone project at AMOLF. I would like to thank my supervisors, dr. Bruno Ehrler (AMOLF, hybrid solar cell group) and dr. Forrest Bradbury (AUC) for their extensive feedback during the project, and my reader dr. Esther Alarcón Lladó (AMOLF, 3D photovoltaics) for taking the time to read this thesis. I am very excited that a prototype of the instrument considered in this thesis is actually being built; I would therefore like to thank ing. Jan Zomerdijk (AMOLF, electronics engineering), ing. Marnix Verwij (AMOLF, mechanical engineering), ir. Ivo Klinkert (AMOLF, software engineering) and others who are, at the time of writing, working on the prototype and who advised me during the project. Furthermore, I would like to thank my group members of the hybrid solar cell group at AMOLF for welcoming me into the group, and for the feedback and help they provided to this project. I remember sitting down at my desk on my first day at AMOLF and blankly staring at my computer screen without a clue on what to do: if it was not for the guidance and help from the aforementioned people I do not think I would have been able to satisfactorily complete this thesis project.

On Wednesday, 13 June at 11:00 I will give a presentation on my project at the AMOLF library, as part of my capstone. Anyone who would wish to do so is welcome to attend.

Throughout this document one will find references to the additional materials, consisting of code files, data files, and other files which supplement this report but which could not be included in the document. The additional materials can be found through [this link](#)¹ or on the AMOLF server: ehrler-group > Group data > Solar Field > merlijn > Thesis.

The code used in this project was written in the Wolfram language using Mathematica 11.2-11.3. It might not run properly on older versions (although it can be opened, and a PDF version of the Notebook code is supplied.). For those not familiar with either the Wolfram language or the Mathematica software, [the online book *An elementary introduction to the Wolfram language* by Stephen Wolfram](#)² offers a good introduction.

In case you find any mistakes in this report, or are left with any inquiries after reading it, please do not hesitate to contact me: kerstenmerlijn@gmail.com.

merlijn Kersten
Amsterdam, May 2018

¹<https://drive.google.com/open?id=1jtmfBJAH4G5J7kjd86wFzULH5XBUwPy>.

²<https://www.wolfram.com/language/elementary-introduction/2nd-ed/>

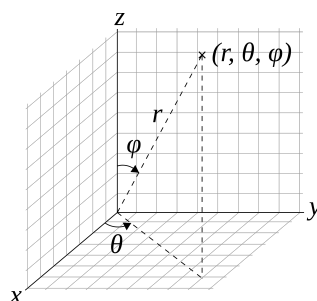


Figure 2: A small remark on notation: throughout this project, the convention for spherical coordinates as depicted in this figure is used; where r is the radial component, θ is the azimuthal angle, and ϕ is the polar angle of a point in (r, θ, ϕ) -space (image source: https://commons.wikimedia.org/wiki/File:3D_Spherical_2.svg).

Contents

1	Introduction	7
1.1	Solar cells	8
1.1.1	Bifacial solar panels	9
1.2	Diffuse irradiation	9
2	Simulation	13
2.1	Methodology	13
2.1.1	Figure of merit	15
2.1.2	Metric	16
2.1.3	Comparison metric and F.O.M.	17
2.1.4	Shading	17
2.2	Results	20
2.2.1	Twelve sensors with shading	21
2.2.2	Relative non-absolute difference	22
2.3	Discussion	24
3	Sensor characterisation	27
3.1	Set-up	28
3.2	Methodology	28
3.3	Results and discussion	29
4	Conclusion and discussion	33
A	Polyhedrons	37
B	Solar simulator versus reference cell	39
C	Code	41

Chapter 1

Introduction

After nearly two centuries of intense fossil fuel use, the world has little time left to stay within its "carbon budget": the maximum amount of greenhouse gasses that can be added to the earth's atmosphere while still having a more than 66% chance of staying below a 2°C (or, alternatively, 1.5° C) rise in global average temperatures [1, 2]. The worst adverse effects of global warming will be averted by keeping temperature increase below this limit. At the time of writing, less than nineteen years are left before reaching this limit of 2°C at current emission rates [1, 2] (and even less time if we want to avoid global warming beyond 1.5°C), so action is needed quickly.

In 2010, 35% of all greenhouse gasses emitted were related to electricity supply, hence this field poses great potential for a reduction in greenhouse gas emissions [3]. Solar energy is one of the most potent renewable energy sources since it is an established and readily available technology. However, there are many types of solar cells, each with their own advantages and shortcomings. By studying the effect of outdoor conditions of various locations on solar cell performance, an informed decision can be made on which type of solar cell would be most suited for use in a specific location. This thesis is concerned with improving an existing instrument that measures the diffuseness of incoming solar radiation, in order to study its effect of different types of solar cells. At the moment, this is not widely studied which is in part due to a lack of reliable and affordable diffuseness measurement tools.

This capstone project was partially carried out as an internship at AMOLF, an institute for functional complex matter research located in Amsterdam Science Park, under supervision of dr. Bruno Ehrler, leader of the hybrid solar cell group. Situated next to the AMOLF building is an array of six different types of solar panels, as can be seen in figure 1.1. It was placed there to study the performance of the different solar cells in Dutch meteorological conditions. In order to do this, proper instruments are needed to measure various parameters, including the diffuseness of incoming solar radiation. Current tools to do this, such as solar trackers (for instance, the [Solys2 sun tracker by Kipp & Zonen](#))¹, are often expensive and can lack in accuracy. They work through two light sensors, one of which is shaded from direct sunlight by a black sphere. The instrument tracks the path of the sun while ensuring that the black sphere is always directly in between the light sensor and the sun. By comparing the output of the two light sensors, the diffuseness of the incoming solar radiation can be determined. Inaccuracies arise, for instance, when direct sunlight is reflected by specular surfaces such as bodies of water or windows. This essentially still direct light will not be blocked by the solar tracker and will thus be registered as diffuse, whereas this should not be the case. Additionally, these devices are expensive and difficult to operate due to the fact that they have to be carefully calibrated to guarantee that they accurately track the position of the sun. Furthermore, they usually only measure

¹For an overview of irradiation measurement tools, see [4, p. 41]



Figure 1.1: A picture of the solar array outside of AMOLF. From left to right, with their respective efficiencies in brackets: copper-indium-gallium-selenium (cIGS, 17.7%), CdTe (12.0%), poly-Si (15.5%), IBC mono-Si (21.5%), SHJ mono-Si (19.4%), cIGS with back mirror (14.7%). In the background, the AMOLF office can be seen.

the diffuseness over a hemisphere whose zenith is the sun, whereas for some technologies, such as bifacial solar panels, the diffuseness all around (on a sphere) the panel has to be known. Therefore AMOLF has been developing their own, cubical diffuseness measurement tool [5]. Tentative results suggest that it works reasonably well, that it is much cheaper to fabricate and that it can properly measure the full diffuseness.

The measurement tool that we consider in this project could further our understanding of the effect of the diffuseness of incoming solar radiation on different types of solar cell radiation and thus help make informed decisions about their use. Another reason for designing the tool that ties in with this is to present a more affordable alternative to currently available diffuseness measurement tools. The underlying rationale is that by creating it, others can also use this tool in their own research. Outside of solar cell research, this tool could also be used for research into lighting design in the built environment [6, 7].

The goal of this project was to improve the accuracy of this measurement tool by increasing the number of sensors on the tool, effectively transforming it from a cube to a higher-order polyhedron. First, we designed a simulation that determines the accuracy of a measurement tool with a given number of sensors. After that, we made a trade-off between accuracy, as calculated through the simulation, and the price of the tool (both of which, in general, increase when the number of sensors increases). We determined that the improved tool should have twelve sensors, after which we further improved the simulation for twelve sensors to more accurately represent the physical reality. Simultaneously, we started building a prototype of the instrument. An important part of this was designing and calibrating the sensors that will be used on the prototype. At the time of writing the prototype was not yet finished, therefore no results from testing it are included in this report. Below one can find a review of theories connected to this project. The next chapter will deal with the simulation, after which the sensor calibration will be covered. This report concludes with a discussion of the results and some appendices giving extra material.

1.1 Solar cells

Solar cells are photovoltaic devices that convert solar energy into electricity. They are often ranked according to their performance under standard test conditions (STC, see for instance the [NREL efficiency chart](#)): under an air mass² 1.5 (AM 1.5) spectrum with a total irradiance of 1000 Wm^{-2} and at a temperature of

²Air mass: a measure of the optical path solar light has to travel through the atmosphere to the face of the earth. When the sun is directly above an observer, the air mass is 1, an air mass of 1.5 corresponds to sun being about 42° above the horizon.

297 K [8][9, p. 22]. These conditions approximate the solar radiation on a sunny day in the continental United States of America during either equinox. However, actual outside conditions vary wildly, depending on parameters such as the time of year, time of day, local meteorological conditions, and more. This affects the solar cell temperature and the spectrum, intensity, diffuseness, and angle of incidence of incoming solar radiation, which are the five main parameters that determine the performance of a given solar cell [10, p. 270].

Under diffuse lighting conditions, the angles of incidence, the intensity and the spectrum of the incoming solar radiation are all altered. In most cases, the incoming solar light will be less intense and its spectrum will be blue-shifted, due to atmospheric scattering by both clouds and airborne particles [11, 12]. This shift can be denoted as a change in the average photon energy, APE, which is the average energy of the photons of a certain spectrum [12]. For the AM 1.5 spectrum the APE is about 1.6 eV [12], if the APE is below this value the spectrum is said to be red shifted, otherwise it is said to be blue shifted (corresponding to the differences in energy of red and blue light, respectively). How these factors affect solar panels differs per type, which in practice means that each type has its own relative decrease in performance. In general, photovoltaic cells with larger band gaps will be more susceptible to spectral effects because of their narrower spectral response [13, 14]. This is due to the fact that solar cells can only absorb light above a certain energy: if, for instance, the spectrum is red shifted, there will thus be fewer photons that can be absorbed. Since each type of solar cell consists of a multitude of layers, each with their own characteristic response to the angle of incidence, there is no simple relation between the angle of incidence and cell performance for different types of cells [10, p. 270], other than that absolute performance decreases when the angle of incidence increases due to higher reflectivity.

1.1.1 Bifacial solar panels

A special type of solar panel is the bifacial solar panel: whereas regular solar panels only collect light on one side of the panels, bifacial panels can collect light on both sides of the panel. These types of panels can therefore achieve higher efficiencies, especially when the panels are mounted vertically or when the panels are elevated above a surface. Through a numerical model, Sun *et al* found that a bifacial solar panel mounted on ground with an albedo³ of 0.25 (such as grass [16]) had an efficiency gain of up to 10% compared to a monofacial panel [16]⁴. This gain can be increased to 30% by increasing the albedo to 0.50 (for instance by covering the ground in white concrete) and elevating the solar panel by 1 m [16]. However, these results were obtained through simulation: it is therefore important that their conclusions are tested experimentally, which could be done using the instrument considered in this report.

1.2 Diffuse irradiation

On average globally, about fifteen percent of incoming solar radiation is diffuse, but this percentage increases in cloudy or hazy conditions [9, p. 22]. In the Netherlands between 1961 and 1980, on average 58% of incoming solar radiation (in energy per square meter) was diffuse [4, p. 54, 72-3]. In clear conditions, the incoming radiation overwhelmingly originates straight from the sun and is therefore called direct or collimated: since the half-angle⁵ of incoming solar light is so small (0.0045 rad [9, p. 263]) that its rays can be considered to be parallel for most practical purposes.

³Albedo: fraction of reflected incident light [15].

⁴Sun *et al* defined gain as a ratio of the yield of bifacial panels, Y_{bi} , and monofacial panels, Y_{mono} : $gain = (Y_{bi} - Y_{mono})/Y_{bi}$.

⁵Half-angle: a measure of angular spread of a light source: if the half-angle is small, it means that a light beam remains concentrated over large distances

Diffuseness occurs most notably due to clouds, but also through scattering due to atmospheric particles, both those occurring naturally or through pollution. It is difficult to predict the incoming diffuse solar radiation at a given time and place, which is why this project is concerned with measuring this quantity. Models to calculate it do exist (see for instance [17, p. 245]), but they too rely on atmospheric input parameters which need to be measured locally, such as the turbidity factor⁶. This makes it impossible to reliably calculate all the relevant details of the incoming solar radiation at a given time and location without doing these measurements and thus it is more straightforward to measure the incoming solar radiation and its diffuseness.

Diffuse light can be categorised in roughly three types. Firstly, there is circumsolar irradiance, which originates from aerosol scattering [16]. This type of scattering produces the ring of white light surrounding the sun, which can be seen when looking up to the sky, see figure 1.2a. A second type of diffuse light is horizon brightening, which is caused by light that reflected of the earth's surface (due to its nonzero albedo) and scattered by the atmosphere. [16]. This light forms the illuminated band above the horizon, which can be seen on sunny days, see figure 1.2b. Another form of diffuse light is isotropic diffuse light, which is also caused by scattering due to aerosols but, in contrast to circumsolar light, comes from all directions equally⁷ [16]. A possible fourth source of diffuse lighting is albedo irradiation: when light is reflected from a non-specular surface, it will be diffuse. This process is similar to that of horizon brightening, but they have to be considered separately due to the fact that light originating from horizon brightening has a different angle of incidence than albedo irradiation and it has a much larger optical path through the atmosphere, which changes its spectrum.

For solar cell research, measuring isotropic diffuse light and albedo irradiation is most important. Circumsolar light has a similar angle of incidence and spectrum as light that is coming directly from the sun and thus has a similar effect on the yield of a solar cell as direct light. Horizon brightening usually does not affect solar cells much because of its low intensity and its small angle of incidence. Isotropic diffuse light and albedo irradiation can substantially affect solar cell yield (as shown in section 1.1.1), mainly due to their higher intensity and because of their different spectra and angles of incidences, which differs significantly from how direct light affects solar cells.

⁶Turbidity factor: a measure for the haziness (or optical depth) of the sky. It depends heavily on local, time-dependent atmospheric conditions, therefore making it especially difficult to incorporate into models (see for instance [18]).

⁷This difference is due to the two different type of scattering mechanism: whereas circumsolar irradiance is caused by Mie scattering, isotropic diffuse light is caused by Rayleigh scattering. For a brief overview of this, see [19]

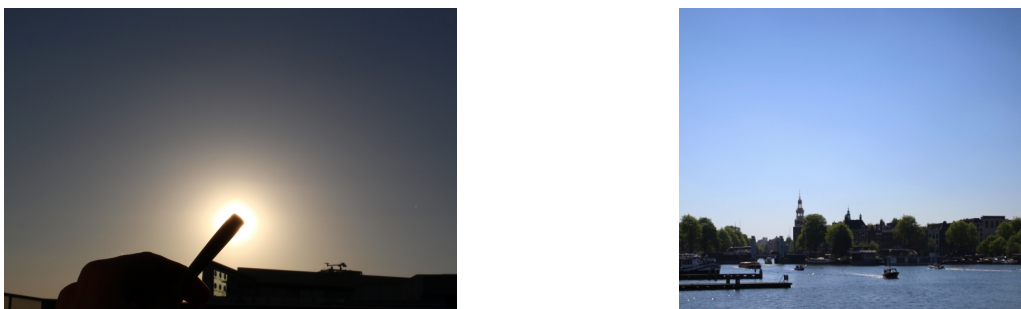


Figure 1.2: a) an example of circumsolar irradiance, which is made visible by blocking the sun's disk. Note the bright aura around the position of the sun's disk, which gradually weakens as the angular distance to sun increases (the abrupt change in brightness close to the sun is due to a overload of the camera sensor). The diffuse lighting effect is enhanced by the fact that this picture was taken shortly before sunset: the longer path of the sun rays through the atmosphere increases the amount of circumsolar irradiance. b) an example of horizontal brightening, as seen from the Nemo science museum looking towards the Prins Hendrikkade in the centre of Amsterdam. Notice how the sky gradually darkens in the vertical direction.

Diffuseness metrics

There are various metrics for diffuseness, each of which has its own applications. An important metric is that of Frandsen, which gives eleven steps of diffuseness (or twenty in the extended model) based on the size of the illuminated object and that of the light source [7]. It is calculated through a spherical probe in a spherical light source, see figure 1.3a. Depending on the angular size, α , of this light source, the ratio of the shaded and illuminated parts of the spherical probe changes from completely shaded ($\alpha = 0$ rad) to completely illuminated ($\alpha = 2\pi$ rad) [7]. In terms of this model, solar radiation under a clear sky would be represented by a small angular size, whereas diffuse solar radiation would have an angular size of approximately π rad. Note that this model does not consider the intensity of incoming solar radiation.

Another diffuseness metric, developed by Cuttle *et al*, uses the flow of light; a measure of both the average direction of light and the strength of the net light transport [6, 7]. The metric is given by the ratio between the light vector, E_v , which denotes the direction of the flow of light, and the illumination scalar, E_s , which represents the ambient light [7]:

$$D_c = \frac{E_v}{E_s} \quad (1.1)$$

Here E_i denotes the illuminance. Note that the name 'vector component' for the quantity E_v is a convention; it is not a mathematical vector. The light vector is defined as the difference in illumination between opposing points of the illuminated object, for example between its top and its bottom [7] (assuming the illuminance is greatest on top):

$$E_v = E_{top} - E_{bottom}.$$

The scalar component E_s gives the average illuminance of the surface of the illuminated object [7]. The Cuttle diffuseness metric ranges from 0 (diffuse) to 4 (direct), but can be normalised as to range from 0 (diffuse) to 1 (direct) (see [7])⁸:

$$D_{c,n} = \frac{1}{4} \frac{E_v}{E_s} \quad (1.2)$$

In this project, a simplified metric based on Cuttle's metric is used, just as was done in the previous project [5]. Similar to Cuttle's measure, it uses the absolute difference in illuminance between opposing points on the surface of the illuminated object, usually taken to be a unit sphere. These values are then divided by the sum of the illuminance over all these points in order to normalise the metric; it ranges from 0 for completely

⁸This can be seen by realising that for a sphere lit by a single light source, one side is always shaded whereas the illumination of a point on the other side is given by $\sin(\phi) \cos(\phi)$. By integrating over the whole sphere and dividing through by the solid angle, 4π , one finds the normalisation factor of 4 [7].



Figure 1.3: a) The theoretical model behind Frandsen's diffuseness metric (from [7]). b) An example of a cubical diffuseness metric tool as described by equation 1.3, with predominantly direct light originating from a point on the positive z axis.

diffuse light to 1 for completely direct light. As an example consider the cubic illumination measurement tool, on which this project seeks to improve [5, 20]. The illuminance is measured over the sides of a cube positioned along the x , y , and z axes, see figure 1.3b. The diffuseness metric is then given by:

$$D = \frac{|E_{+x} - E_{-x}| + |E_{+y} - E_{-y}| + |E_{+z} - E_{-z}|}{E_{+x} + E_{-x} + E_{+y} + E_{-y} + E_{+z} + E_{-z}} \quad (1.3)$$

This measure is approximately equal to the normalised Cuttle metric $D_{c,n}$. It can be generalised for a measurement tool with an arbitrary number of opposing sides which are labelled by the subscript i :

$$D = \frac{\sum_i |E_{+i} - E_{-i}|}{\sum_i E_{+i} + E_{-i}} \quad (1.4)$$

This is the diffuseness metric that will be used in this report.

Chapter 2

Simulation

This chapter gives a description of the code used to simulate the diffuseness measurement tool, which can be found in the additional materials and in appendix C. The aim of the code was to calculate the accuracy of a diffuseness measurement tool (using equation 1.4) with a certain number of sensors, illuminated by light with a certain diffuseness fraction. In general, the accuracy of the instrument increases as the number of sensors increases. Therefore, the figure of merit, F.O.M. (the value to which the metric value will be compared) was chosen to be the value given by an instrument in the limit of the number of sensors going to infinity, see section 2.1.1. In the following sections, we will give the assumptions made in the model, outline the various calculations done by the code, and discuss the results that they yield.

2.1 Methodology

The actual instrument will consist of a polyhedron of around ten centimetres in width, with sensors on each face, see figure 2.1a. It will be surrounded by two transparent hemispheres with a diameter of around thirty centimetres, which are held in place by an opaque ring, which is connected to the polyhedron through three rods. It will be placed on a pole at a height of about two metres next to the AMOLF solar array, see figure 1.1.

In the code, the measurement tool and its environment are highly simplified. The instrument itself is taken to be a unit sphere centred around the origin. The sensors are points on this sphere (see figure 2.1b). Incoming light is represented by a diffuse and a direct vector field, both of which have a maximum

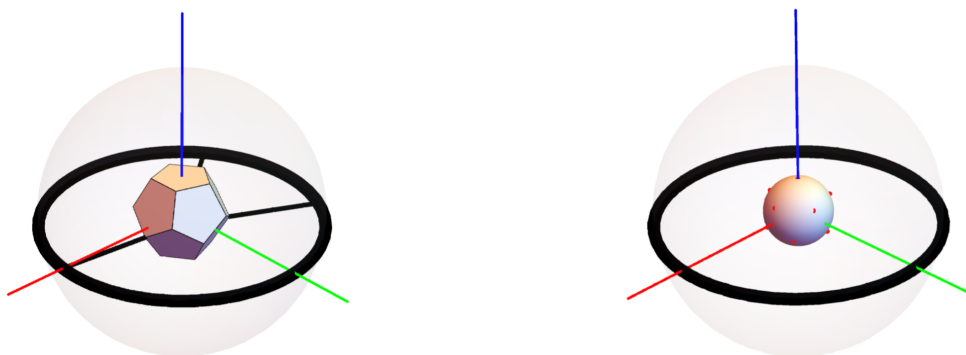


Figure 2.1: Two mock models of the measurement tool for twelve sensors: a) a realistic model (dodecahedron), the sensors would be in the middle of the faces; b) the model used in the code for twelve sensors, where the red dots denote the locations of the sensors. The shadow of the ring (not shown here) is only taken into in section 2.1.4. The red lines denote the x axis, the green lines denote the y axis, and the blue lines denote the z axis.

magnitude of one. The direction of this vector field is towards the light source and thus hence away from the sensors: although this does not represent the actual physical situation where light goes from the light source to the sensors, but it yields the same results and was easier to implement in the code. All references to "light" or "light field" in this chapter refer to this inverted light scheme.

The code considers isotropic diffuse lighting only. If we consider a point on the unit sphere, this light, when thought of as a vector field, would be extending outwards in all directions with equal magnitude, effectively forming a hemisphere centred on the point; see figure 2.2a. However, since this was too difficult to implement, the code uses a single vector extending radially outwards from the point figure 2.2b. This simplification can be seen as an average: due to the symmetry of the vectors in figure 2.2a, their average would have the direction of the vector in figure 2.2b. This "average vector" does not take into account the magnitude of the vectors of figure 2.2a, but is instead normalised to one¹. This unit radial vector of the point considered is then multiplied by a fraction (the parameter `fraction` in the code) which refers to the fraction of diffuse light where 0 signifies a fully direct light field and 1 a fully diffuse light field².

The direct field extends from the origin to the light source, whose position is denoted by the parameter `coordinates`. The coordinates of the position of the light source are normalised to simplify calculations, this does not affect the vector field since it is the direction that matters and this remains unchanged through this normalisation. The direct field is defined by multiplying the direct-fraction ($1 - \text{fraction}$) by the normalised coordinates of the direct light source.

```
direct:=(1 - fraction)*Normalize[coordinates];
diffuse[{a_, b_, c_}]:=fraction*Normalize[{a, b, c}];
```

Listing 2.1: Definition of the light vector fields. The `diffuse` function takes as input the coordinates of a point $((a, b, c))$.

A measurement of the illuminance, E , of either vector field at a certain point is taken to be the dot product of the respective vector field (whose absolute magnitude is at most one) and the unit normal vector of the point on the sphere³. To account for the fact that light cannot go behind the sensor (since it will be shaded by the instrument itself), the measurement is only done when the dot product is larger than zero⁴. In later sections other forms of shading will also be taken into account (see section 2.1.4). The dot products

¹Therefore, when considering diffuse light, this model ignores effects arising from the fact that the sensors have a nonzero area which leads to a angle-dependence of the dependence of the sensor output on the light intensity. However since the diffuse light is assumed to always be completely isotropic this should not introduce a large error. The dependence of sensor output on the angle of incidence is taken into account for the direct light field.

²Note that this diffuseness fraction is simply the maximum magnitude of the diffuse light, whereas the diffuseness of solar radiation refers to the ratio between diffuse light and total solar radiation [4, p. 70]

³See the first section of chapter 3 for an experimental verification of this approach.

⁴Note that due the definition of the diffuse light, this does not affect this light field. However, in order to allow for future improvement of the model this condition was implemented in the code for both light fields

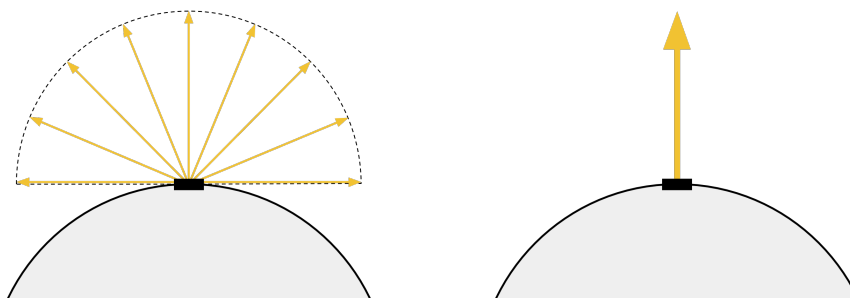


Figure 2.2: a) a realistic depiction of diffuse light, extending outwards from a point on the sphere (black rectangle). b) the approach used in this report, showing the single radial vector.

of the diffuse and direct fields are taken separately and added to form the illuminance measurement. In this way, they cannot extinguish each other (just as is the case with real light), something which would be possible if they were summed before the dot product was taken.

```
illuminance[d_]:=If[Dot[diffuse[d],Normalize[d]]>=0,Dot[diffuse[d],Normalize[d]],0]+
If[Dot[direct,Normalize[d]]>=0,Dot[direct,Normalize[d]],0];
```

Listing 2.2: Illuminance calculation, which takes as input the coordinates of the sensor points (denoted by d).

This illuminance is used to calculate the diffuseness metric as given by equation 1.4. In the code, the vector quantity is first calculated for every sensor point on the sphere, its antipode is found by taking the negative of the coordinates of this sensor point. This means that the sum over the coordinates counts every antipode-pair twice and hence the final metric is divided by two to correct for this, just as in equation 1.4.

```
vector[e_]:=Abs[illuminance[e]-illuminance[-e]];
metriccalculation=0.5*Sum[vector[f],{f,normals}]/Sum[illuminance[g],{g,normals}]
```

Listing 2.3: Metric calculation, which takes as input the coordinates of the sensor points, denoted by e , f and g .

When calculating the metric or the figure of merit (see next sections), the absolute value of the z -component is always used. This is done to more accurately simulate the sun's position, which cannot be below the horizon (taken to be the $z = 0$ plane). In the sections below, the code is explained step-by-step: in order to view the full code one can either download it from the additional materials or view it in appendix C.

2.1.1 Figure of merit

As said before, the figure of merit is taken to be the value of the metric, given in equation 1.4, in the limit when the number of sensors goes to infinity. In this case, the sensor point will form the surface of the unit sphere, given by $x^2 + y^2 + z^2 = 1$. Therefore the figure of merit, F.O.M. is found by integrating the metric over the unit sphere:

$$\text{F.O.M} = \frac{1}{2} \frac{\int_R |E(x, y, z) - E(-x, -y, -z)| dA}{\int_R E(x, y, z) dA} \quad (2.1)$$

Where E denotes the illumination of a point and R is the surface in (x, y, z) -space such that $x^2 + y^2 + z^2 = 1$. The factor of $\frac{1}{2}$ is included since this integration considers each point twice: once as a solution (x, y, z) of the relation $x^2 + y^2 + z^2 = 1$ (first part of the numerator) and once as the negative of its antipode $(-x, -y, -z)$ (second part of the numerator).

In the code, the figure of merit as given by equation 2.1 is implemented by defining a function `figureofmerit` that takes as arguments the fraction of diffuse light (`fraction`) and the position of the direct light source (`coordinates`). It then uses these parameters to define a direct and a diffuse vector field with strength given by the parameter `fraction`. Next it checks whether the point is shaded by the instrument by taking the dot product between the position of the light source and the position of the point: if it is greater than or equal to zero, it calculates the illumination; if it is less than zero it returns a zero illumination value. This is then used to calculate the figure of merit, given by equation (2.1), through numerical integration over the unit sphere.

```
figureofmerit[fraction_,coordinates_] := Module[{} ,
Which[coordinates[[3]]<0, coordinates[[3]]=Abs[coordinates[[3]]];
direct:=(1-fraction)*Normalize[coordinates];
```

```

diffuse[a_, b_, c_] := fraction * Normalize[{a, b, c}];

illuminate[d_, e_, f_] := If[Dot[diffuse[d, e, f], Normalize[{d, e, f}]] >= 0, Dot[diffuse[d, e, f], Normalize[{d, e, f}], 0] +
  If[Dot[direct, Normalize[{d, e, f}]] >= 0, Dot[direct, Normalize[{d, e, f}], 0];

figure = 0.5 * NIntegrate[Abs[illuminate[d, e, f] - illuminate[-d, -e, -f]], {d, e, f} \[Element] Ball[{0, 0, 0}, 1]] /
  NIntegrate[illuminate[d, e, f], {d, e, f} \[Element] Ball[{0, 0, 0}, 1]]
]

```

Listing 2.4: Figure of merit code, it takes as parameters the coordinate of the light source (`coordinates`) and the fraction of diffuse light (`fraction`).

This code is then used to calculate the figure of merit for eleven values of the diffuse-fraction between 0.0 and 1.0 in steps of 0.1. The parameter `coordinates` can be chosen at random, since it does not affect the outcome of the calculation: it is completely spherically symmetric and thus each value of `coordinates` yields the same value. See table 2.1 in the next chapter for the calculated values.

2.1.2 Metric

The metric as defined in the previous chapter calculated the absolute difference in illumination, E , of antipodes on a sphere and divides by the total illumination, which yields a figure between 0 (diffuse light) to 1 (direct light):

$$D = \frac{\sum_i |E_{+i} - E_{-i}|}{\sum_i E_{+i} + E_{-i}}$$

The metric calculation requires three variables: the number of sensors (`points`), the fraction of diffuse light (`fraction`), and the coordinates of the light source (`coordinates`). The metric calculation function begins by defining the two vector fields used, in the same way as for the figure of merit.

We wanted to calculate the metric for eleven different numbers of sensor points between 6 and 26 in steps of 2. In order to do this, we needed the coordinates of these sensor points. To get the best results, the antipode pairs had to be distributed uniformly over the unit sphere. This problem is similar to the Thomson problem and related Tammes problem, which are concerned with uniformly distributing electrons and circles, respectively, over a sphere. There are some exact solutions to this problem (for $n = 3, 4, 6, 12$ [21]), some of which were used in this report ($n = 6, 12$). When no exact solutions were available, or when they did not suffice (for instance because the points of the solutions were not antipodes), approximate solutions were used by comparing different polyhedrons with the required number of vertices, based on whether the points were antipodes and whether the points were distributed uniformly (approximately). The coordinates of these vertices were then used as coordinates of the sensor points; see appendix A for a complete list of polyhedrons used. After this, these points were used to calculate the illuminance, again in a similar manner as in the figure of merit. Lastly, the metric as defined by equation 1.4 was calculated by first calculating the vector component and then calculating the actual metric. This value was then returned.

```

metric[points_, fraction_, coordinates_] := Module[{} ,
  Which[coordinates[[3]] < 0, coordinates[[3]] = Abs[coordinates[[3]]];

  direct := (1 - fraction) * Normalize[coordinates];
  diffuse[{a_, b_, c_}] := fraction * Normalize[{a, b, c}];

  Which[
    points == 6, normals = Normalize[#] &/@ PolyhedronData["Octahedron", "Vertices"],
    points == 8, normals = Normalize[#] &/@ PolyhedronData["Cube", "Vertices"],
    points == 10, normals = Normalize[#] &/@ PolyhedronData["ElongatedSquareDipyramid", "Vertices"],
    points == 12, normals = Normalize[#] &/@ PolyhedronData["Icosahedron", "Vertices"],
    points == 14, normals = Normalize[#] &/@ PolyhedronData["CumulatedCube", "Vertices"],

```



```

points==16,normals=Append[Append[Normalize[#]&/@PolyhedronData[{"Antiprism",7},"Vertices"],{0,0,1}],{0,0,-1}],
points==18,normals=Normalize[#]&/@PolyhedronData["OctahedronThreeCompound","Vertices"],
points==20,normals=Normalize[#]&/@PolyhedronData["Dodecahedron","Vertices"],
points==22,normals=Normalize[#]&/@PolyhedronData["Rhombicuboctahedron","Vertices"],
points==24,normals=Normalize[#]&/@PolyhedronData["SmallRhombicuboctahedron","Vertices"],
points==26,normals=Normalize[#]&/@PolyhedronData["DisdyakisDodecahedron","Vertices"]
];

illumiance[d_]:=If[Dot[diffuse[d],Normalize[d]]>=0,Dot[diffuse[d],Normalize[d]],0]+
If[Dot[direct,Normalize[d]]>=0,Dot[direct,Normalize[d]],0];

vector[e_]:=Abs[illumiance[e]-illumiance[-e]];

metriccalculation=0.5*Sum[vector[f],{f,normals}]/Sum[illumiance[g],{g,normals}]
]

```

Listing 2.5: Function that calculates the metric for a certain position of the direct light field (`coordinates`), number of sensors (`points`), and diffuse-light fraction (`fraction`). Note that the vertices of the polyhedrons are used, not their faces.

2.1.3 Comparison metric and F.O.M.

In order to compare the calculated values of the metric, D , to the figure of merit, F.O.M., the relative absolute difference between them was calculated:

$$\text{difference} = \frac{|D - \text{F.O.M.}|}{\text{F.O.M.}} \quad (2.2)$$

This yields a number between 0 and ∞ , where a zero value means that both measures are equal and a nonzero value gives the percental change in the metric with respect to the figure of merit. As such, it gives an indication of the error of the metric for a given number of sensors. This approach does not work for a diffuseness fraction value of 1.0, since the figure of merit is 0 for these values and thus the difference is infinite.

The relative absolute difference, rather than the absolute difference, was used because it gives a much better indication of the actual error. This is because the figure of merit changes between 0 and 1, depending on the diffuseness fraction: therefore an absolute difference of, for instance, 0.2 might be small for highly direct light, but large for highly diffuse light: by dividing through by the figure of merit this ambiguity is removed, making it easier to compare the accuracy of the instrument for different diffuseness fractions.

2.1.4 Shading

By using the code described in the previous sections, it was decided that the measurement tool would have twelve sides (for more information, see section 2.2). After this decision was made, the model for twelve points was developed further in order for it to be more realistic. An important part of this was to include the shadow of the ring (shown in the models in figure 2.1) on the sensors in the model. This was done both for the diffuse and the direct light field. Furthermore, the exact coordinates of the sensors on the actual instrument were used as coordinates for the sensor points in the code. The calculations below are given for the case of twelve sensors, but the same method could be applied to any number of points. This was not done, because it would very time consuming to adapt the model and it would not contribute significantly to the project. Note that both shadow functions given below include the aforementioned case in which the instrument itself is between the light source and the sensor, thus causing shading.

Diffuse light field

The ring does not shade the diffuse light field of the top and the bottom sensor: all diffuse light going outward from these sensors would not be shaded by the ring, because the ring is either below or above the

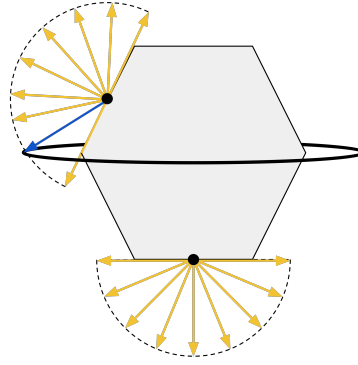


Figure 2.3: Two dimensional representation of shading for the diffuse lighting field: as can be seen, the bottom sensor (represented by the black point) is not shaded, whereas the side sensor is partially shaded (blue arrow).

sensor (see figure 2.3). For the other sensors, one has to consider the angular surface of the ring: when the light field extends outwards from the sensor in a hemisphere, a fraction of the light will be shaded by the ring. This fraction is proportional to the angular size of the ring. The shading is thus defined as the ratio between the angular size of the ring (as seen from the sensor) compared to the total angular size of the hemisphere, 2π (see figure 2.3 for a simplified, two-dimensional model). This shading is implemented by multiplying the unit light vector by the shading function. This disregards the slight change in the direction of the incoming diffuse light, but it is correct to first order. Because the polar angle between the equator of the sphere and the sensors on the side is the same for all of them ($|\phi_{sensor} - \pi/2| = 0.4632$ rad), they also all experience the same shading. For the prototype, the ring will have a radius of approximately 15 cm and a width of approximately 1 cm. Therefore the sensors on the side of the instrument will receive about 2.6% less diffuse light than the top and bottom sensors when shading is considered.

```
shadediffuse[h_]:=If[Dot[diffuse[h], Normalize[h]]>=0, If[h!={0,0,1}&&h!={0,0,-1}, 0.974, 1], 0];
```

Listing 2.6: Diffuse light field shading function, it takes as argument the coordinates of a sensor (\mathbf{h}) on the unit sphere and returns a shading factor of $1 - 0.026 = 0.974$ when the sensor is partially shaded by the ring.

Direct light field

The shading of the direct field is slightly more complicated. To find out if a certain sensor is shaded by the ring, one has to compare the unit vector of the direct light field with a unit vector from the sensor to the ring. If these unit vectors (almost) coincide, the sensor will be shaded by the ring. The unit vector from the ring to the sensor can have any possible azimuthal angle (see figure 2.4b), since the ring describes a full circle around the sphere on which the sensor is. In order for the sensor to be shaded, the azimuthal angle of the sensor-to-ring vector needs to be nearly the same as that of the direct light field (see 2.4b). The polar angle of the sensor-to-ring vector is given by subtracting the sensor vector from that of the ring ($\phi_{ring} = \pi/2$, see 2.4a). If the dot product between the unit vector of the sensor-to-ring vector and the direct light vector is (nearly) equal to one, the sensor will be shaded.

A small deviation of this value is allowed, to account for the width of the rim. For the model, the cut-off value of the dot product was taken to be 0.9983 which corresponds to a ring with a width of approximately 1 cm. For the figures (such as 2.4), a lower cut-off value was used since it showed the shading function more clearly. Figure 2.4c,d show images from a three dimensional representation of the shading function applied to a model of the instrument (it can also be found in the additional materials). In these images, one can see how the shadow of both the ring and the instrument itself is distributed over the instrument's surface.

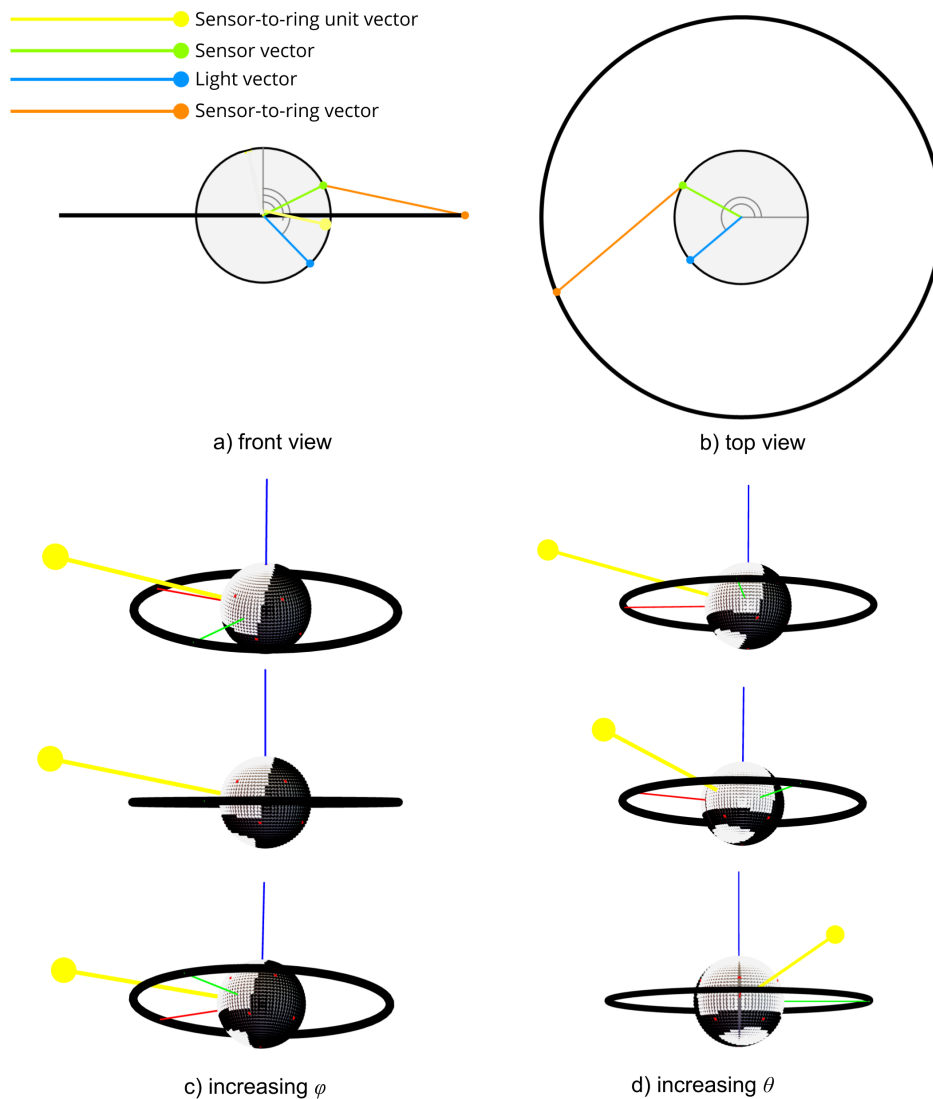


Figure 2.4: a,b) two-dimensional models of the direct shading functions. The green vector gives the normal vector of the sensor, the blue vector gives the unit vector of the light field, the orange vector gives the line from the sensor to the ring that would cause shading, and the yellow vector gives its unit vector. a) shows a front view and thus gives the ϕ -dependence of the shading function. b) shows a top view and thus gives the θ -dependence of the shading function. Note that the blue and orange line are parallel and note that the yellow sensor-to-ring vector is not drawn in this plot, since it coincides with the blue light vector. c,d) show models of the shading function, where black points are shaded and white points are not. The yellow line gives the position of the light source, the red, green, and blue lines give the x , y , and z axes (respectively). c) shows the model when it is rotated in the z plane, or in spherical terms when ϕ is increased. d) shows the model when it is rotated in the (x, y) plane, or when θ is increased. In the additional materials, three dimensional models and an animation of the model in c,d) are supplied.

```
shadedirect[i_, j_] = Module[{},
  pointtorim := tocartesian[{1, tospherical[i][[2]], tospherical[tocartesian[{3, tospherical[i][[2]], Pi/2] - j][[3]]}];
  shadecalulation = If[Dot[Normalize[i], j] > 0 && Abs[Dot[Normalize[i], pointtorim]] < 0.9983, 1, 0];
  returns = If[NumericQ[shadecalulation], shadecalulation, 0];
];
```

Listing 2.7: Direct light field shading function, it takes as arguments coordinates of the light field (i) and the coordinates of a point on the unit sphere (j).

2.2 Results

Calculations of the figure of merit yielded the results given in table 2.1 and figure 2.5a. As can be seen, the results are skewed towards lower metric values and thus more diffuse lighting conditions. Other studies, such as [22], have found a more even distribution of metric values using a more realistic manner of defining the diffuseness fraction, as can be seen in figure 2.5b. This suggests that the way the diffuseness fraction is defined in this report does not accurately represent the physical reality, which means that the results for a certain diffuseness ratio as defined in this report cannot be readily translated into a real-life diffuseness value, as was touched upon in section 2.1.

Fraction	0.0	0.1	0.2	0.3	0.4	0.5	0.6	0.7	0.8	0.9	1.0
F.O.M.	1.000	0.6923	0.5000	0.3684	0.2727	0.2000	0.1429	0.09677	0.05882	0.02703	0.0000

Table 2.1: Value of the figure of merit for different fraction values. Both measures are dimensionless.

The calculation of the comparison between the metric and the figure of merit for the eleven different number of sensors given in table 2.1 yielded the values given in figure 2.6a. The markers representing 6, 12 and 24 points are highlighted using connecting lines, because 6 points represents the original cube, 12 points represents the number of points chosen for the prototype of the instrument, and 24 points represents the most accurate model (in the calculated range of the number of sensors).

The comparison value was calculated using 4,000 random coordinates of the light source per pair of diffuseness fraction value and number of sensors. In previous, similar versions of the code, increasing the number of random coordinates beyond 2,000 did not significantly change the accuracy of the simulation, it was assumed that the same is true for the current version of the code. One indicator of this is the smoothness of the lines connecting the data markers: it was observed that as the number of random

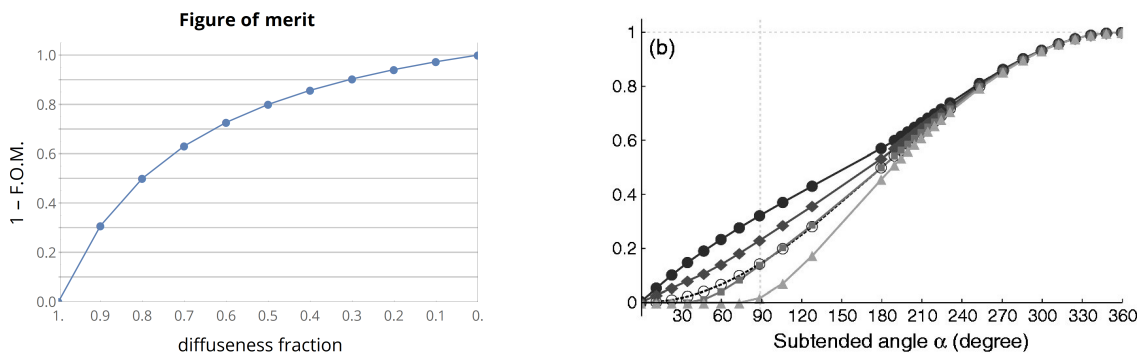


Figure 2.5: a) figure of merit data as given in table 2.1. Note that this figure gives the value of $1 - \text{F.O.M.}$ and that the x -axis is inverted. This was done to facilitate comparison with figure b) which uses an inverted version of the Cuttle's diffuseness metric. Thus in both figures, a metric or $1 - \text{F.O.M.}$ value of 0.0 signifies a fully direct light source ($\text{fraction} = 1.0$ or $\alpha = 0^\circ$) and a value of 1.0 signifies a fully diffuse light source ($\text{fraction} = 0.0$ or $\alpha = 360^\circ$). b) Cuttle's metric as calculated (open data points) and measured (different orientations, filled data points) for a probe in spherical light as given by 1.3a [22].

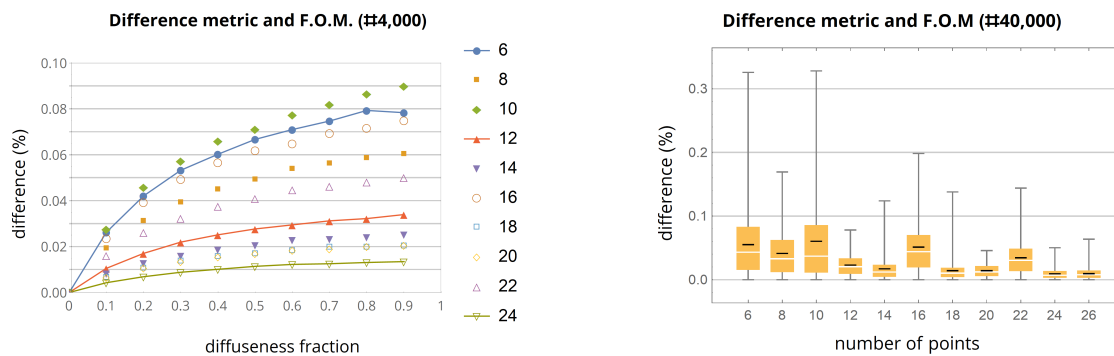


Figure 2.6: a) The absolute relative difference between the metric and figure of merit (see equation 2.2) for various numbers and various diffuseness-fractions. b) box plot of the mean value of the absolute relative difference between the metric and the figure of merit for various numbers of points over the various diffuseness fractions. The black line depicts the mean value. Plot a) was calculated with 4,000 random coordinates of the light field per data point, for plot b) these data points were combined such that each individual box plot represents calculations done with 40,000 random coordinates of the light field.

coordinates used increased, the lines became more smooth. Since the lines for 4,000 points are almost completely smooth, this serves as an indicator that the number of random coordinates used is high enough to give accurate results.⁵

The graphs in figure 2.6 show that, on the whole, the accuracy of the metric increases as the number of measurement points increases. However, this correlation is not perfect: the most accurate (in terms of both smallest mean and the 75% interval) is that of 24 points, and some number of sensor points (most notable 10, 16, and 22) give significantly worse results than their predecessors. This is probably due to an uneven distribution of the sensors over the sphere, which is often because there is no perfect solution for uniformly distributing that number of points over a sphere (see 2.1.2). However, virtually all number of sensors (except for $n = 10$) give better results than the original cube ($n = 6$), on which this project tries to improve. The shape of the graph indicates that for all different number of points, the metric as calculated by the instrument becomes much more accurate when the incoming solar radiation is more direct. This might be due to the fact that gradual changes in light intensity for diffuse light cannot be measured correctly by a limited amount of points: instead, the light intensity varies abruptly from sensor to sensor causing a larger error.

Due to the aforementioned discrepancy between the diffuseness fraction used in this report and the actual diffuseness of incoming solar radiation, it is difficult to predict the behaviour of the instrument in outside-conditions. However, the data does imply that the accuracy worsens as the amount of diffuse light increases, which means that the sensor will perform worse in places with high diffuse incoming solar radiation, such as the Netherlands, than in places with less diffuse incoming solar radiation.

2.2.1 Twelve sensors with shading

After taking into consideration the mean relative absolute difference and various other parameters, it was decided that the measurement tool would have twelve sensors. An important consideration was the fact that the error due to the reflectiveness of the transparent sphere surrounding the instrument would be about four percent: a smaller mean error of the instrument itself would thus not have increased the overall accuracy much. Other important considerations were the ease of manufacturing and the cost of the prototype.

The effect on the metric calculation due to the changes in the improved model for twelve sensors, which

⁵Note that the number of random coordinates cannot be increased much beyond 5,000 due to limitations in computing capacity.

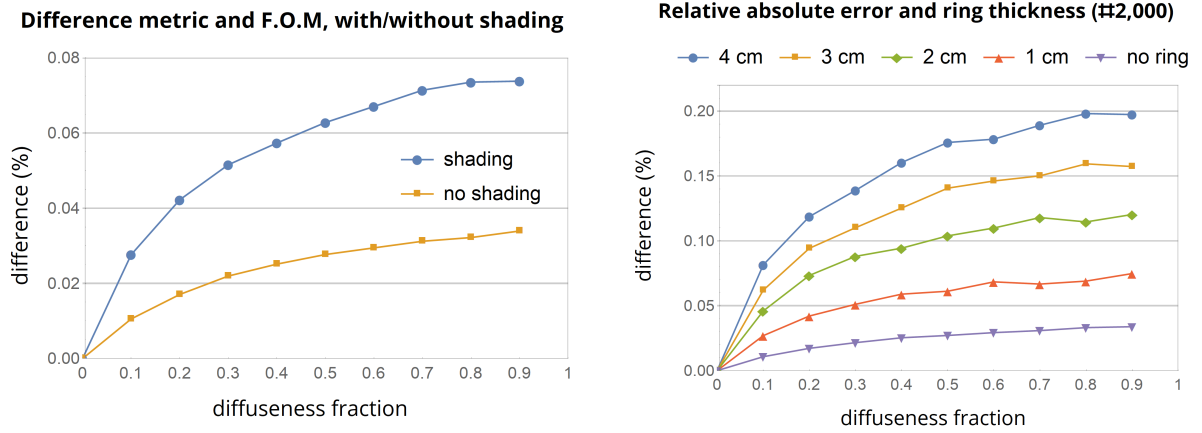


Figure 2.7: a) The relative absolute difference between the metric and the figure of merit for a sensor with twelve points, with and without shading calculated for 10,000 and 4,000 data points, respectively. b) The relative absolute difference between the metric and the figure of merit for a sensor with twelve points with shading, for four different values of the ring thickness and without a ring present. The red triangles represent the data points of the ring-size that corresponds to that of the prototype.

takes into account shading as described in section 2.1.4, is given in figure 2.7a. It compares the relative absolute difference between the metric and the figure of merit for a measurement tool with twelve sensors with and without shading. Note that the figure of merit is calculated without taking into account shading due to the ring: as noted in section 2.1.4 implementing the shading functions for a given number of points is a difficult and lengthy process, and it was deemed unfeasible to do this for the figure of merit calculations, which considers an infinite number of points. As can be seen in the plot, the shading reduces the accuracy of the model, in terms of the mean difference. However, the difference is still much smaller than that of the original cube (see figure 2.6a).

The shading function depends heavily on the width of the ring, as shown in figure 2.7b. Therefore decreasing the width of the ring would significantly reduce the error in the metric measurement. Another option, one which will be used on the prototype, is to use a semi-transparent ring (the model assumes a completely opaque ring). This option could not be modelled, since it is unknown exactly how the ring scatters light. However, we are confident that it reduces the effect of the ring on the diffuseness measurement, and thus the error in the diffuseness measurement as given in figure 2.7a will most likely be smaller for the prototype.

2.2.2 Relative non-absolute difference

So far, this document has only considered the absolute relative difference between the metric and the figure of merit, as defined in equation 2.2, since this property has the most practical value. However it is also interesting to look at the non-absolute relative difference, since it depicts the spread in difference values more faithfully. It is given by:

$$\text{difference} = \frac{D - \text{F.O.M.}}{\text{F.O.M.}} \quad (2.3)$$

A box plot of this value for different fraction values is given in figure 2.8a. It shows that most difference values are distributed around the x -axis but with large, negative outliers. The median relative difference value is close to zero, while the mean difference value is slightly negative. Figure 2.8b shows the number of counts for small intervals of the difference value, for different diffuseness fraction values. It shows similar behaviour to figure 2.8a, with the highest number of counts around the x -axis and with large outliers. This figure also shows that these outliers consists of different modes: four to five different modes can be

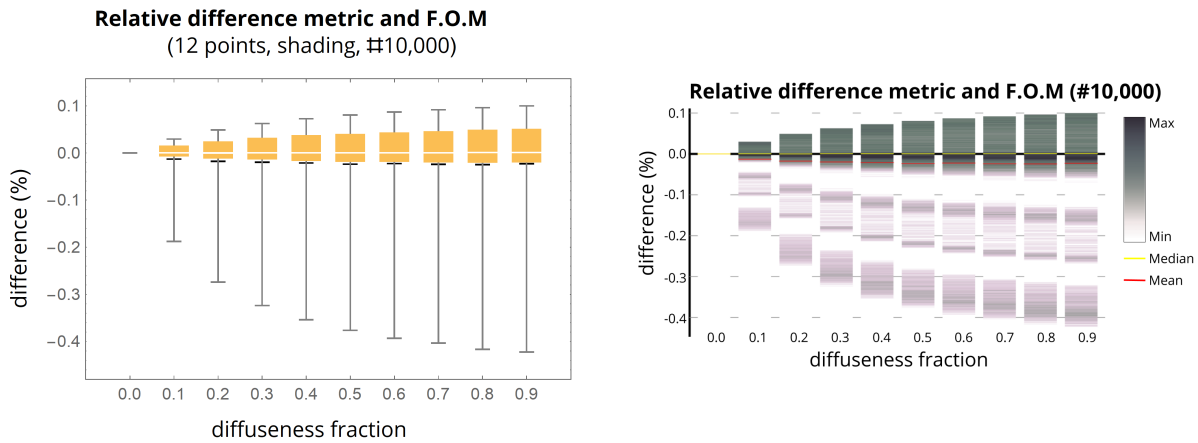


Figure 2.8: a) a box plot of the relative difference between the metric and figure of merit, calculated for an instrument with twelve sensor with shading for various fraction values, using 10,000 random coordinates of the light source per fraction value. b) a density plot of the 10,000 measurements for a shaded instrument with twelve sensors for different diffuseness fraction values, showing the relative difference ordered by data point for the same data as in plot a). The darker the difference interval, the higher the number of counts. Note the modes that are clearly visible. The higher the count in figure 2.9, the darker the line in plot b).

distinguished in the plot. Figure 2.9 shows the results of calculating the relative difference according to equation 2.3 for twenty thousand points with a diffuseness fraction value of 0.9⁶. The number of counts within a small difference interval in figure 2.9 determines the colour of the lines in figure 2.8b: the higher the number of counts in the first plot, the darker the line in the second plot. The colour of the dots signify for how many sensors the direct light field was shaded by the ring due to the random position of the light source, ranging from one shaded sensor to more than five shaded sensors⁷. The grey dots signify positions for which the direct field was not shaded due to the ring for any sensor. Note that for each point the diffuse light field was shaded by the ring for ten of the sensors at all times. This plot shows that in most cases, shading of one or more sensors causes the the metric to be smaller (more diffuse) than the figure of merit, which causes the relative difference to be negative, although this does not seem to be a general trend, as can be seen in the points with shading above the x -axis. However, as the number of shaded points increases, the difference does become more negative in many cases: this can most clearly be seen in the many green, yellow, orange and red points below the relative difference value of -0.3 .

Note that the plot shows that the different modes are mainly a result of the number of sensors shaded by the ring: this is especially clear for the case when five or more sensors are shaded (the red dots), the data points of which form a mode around -0.4 . This might be due to the fact that there is probably only one type of symmetry that causes five or more sensors to be shaded: this symmetry has a certain error in the metric value, and thus metric values calculated for this symmetry have a similar difference value. The spread in this difference value (the width of the mode in the plot) is due to the thickness of the ring, which means that there is a small range of positions of the light source which induce shading for five or more sensors.

The other number of shaded sensors all have multiple modes: for instance, the green dots (two shaded sensors) have two modes: around a difference value of 0.0 and around a difference value of -0.35 . This could be due to the fact that there are two different symmetries of the position of the light source with respect to the instrument that cause two sensors to be shaded, both of which have a different difference

⁶Note that figures 2.8ab and 2.9 were made using different data points generated by the same code. Therefore there might be small differences between the plots.

⁷In practice, this almost always meant five sensors were shaded, it is difficult to shade more due to symmetry. The number of shaded sensors does not take into account shading causes by the instrument itself.

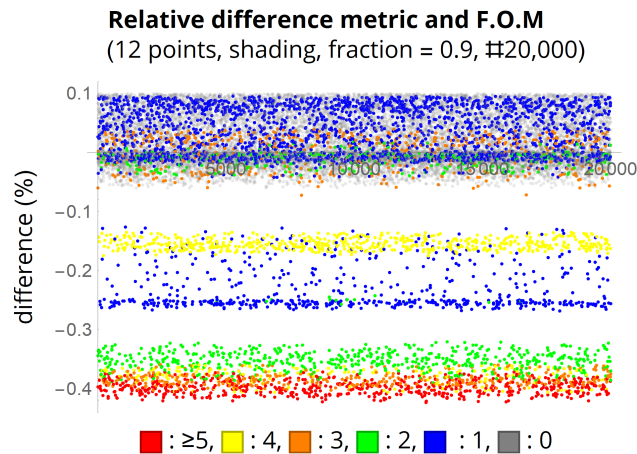


Figure 2.9: A plot of the relative difference between the metric and figure of merit value for an instrument with twelve point for light with a diffuseness fraction of 0.9 with shading, calculated for 20,000 random coordinates of the direct light field. The colour of the data points indicates the number of sensors shaded by the ring for the direct light field.

value. This may also explain why the blue dots (one shaded sensor) are less obviously divided into modes: there are many configurations that cause one sensor to be shaded, all of which have very different difference values.

Most of colour modes are very clearly demarcated, which can for instance be seen for the mode of the grey dots (no shaded sensors), which ends abruptly around a difference value of 0.1. This is likely due to fact that for positions of the light that cause a difference value of around 0.1, a small change might mean no shading (a grey dot, below 0.1) or shading of at least one sensor (a coloured dot, in another mode). This can only be known for certain when the coordinates of the light source for the data points in plot 2.9 are known, which is not the case at the moment.

2.3 Discussion

The code as outlined above still has some shortcomings. The measurement tool is taken to be in empty space; hence diffuse light is coming from all directions equally, contrary to the real-life situation where the diffuse field is significantly stronger on the side of the instrument facing the sky. It is unclear how this difference affects the simulation, this could be explored in a new project. Furthermore, the model only takes isotropic diffuse irradiance into account, not the other forms of diffuse irradiation. It is thought that omitting circumsolar irradiance, horizon brightening or albedo irradiance does not cause major errors, due to the fact that the instrument will be surrounded by buildings on most sides which block any irradiance due to horizon brightening and because the grass on which the instrument is situated has a low albedo value of 0.25 [16]. Furthermore, circumsolar irradiance comes from the same direction as sunlight which has a much higher intensity, thus its relative contribution to the total measurement is much smaller.

The model does not take into account any reflections due to the surfaces of the transparent sphere surrounding the instrument and the instrument itself, nor shading or reflections due to the rods that connect the ring and the sphere to the instrument (see figure 2.1). The actual model will be placed next to the solar array outside of the AMOLF office, where various objects will cause shading and reflection during the day: none of this was taken into account in the model. Besides that, the polyhedrons chosen for the point coordinates (see appendix A) might not be optimal and thus the values given in figure 2.6 might be an over-estimation (for instance for 10 and 22 sensor points). However, any deviations this may cause are expected to be small, and it is difficult (or impossible) to mathematically rigorously determine the best configuration.

This is partly due to the large number of polyhedrons with a given number of vertices. This might particularly effect $n = 10, 16, 22$ which showed difference values deviating from the general trend. However, any deviation from the values given in the plots are expected to be small. Thus the observed trend in error value as a function of the number of sensors is thought to be unaffected.

Despite these short-comings, the model will not be improved further, but instead, our attention was focused on preparing the sensors for the prototype which is being built at the moment (see next chapter). The current model could be a starting point for a new project which would aim to make a more realistic value of the error in the metric value for a given number of sensor points.

Chapter 3

Sensor characterisation

This chapter is concerned with characterising the light sensors that will be used on the prototype of the measurement tool. The sensors consist of a small PCB which contains a temperature sensor, a light sensor, and some electronic parts such as a memory piece, see figure 3.1b. The light sensor can measure the intensity (given in counts) of red, green, blue and infrared light. It also measures the total (or 'clear') light intensity. The light sensors used are ams TCS3400 Color Light-to-Digital Converter sensors [23].

In the simulation (see section 2.1), the angle-of-incidence dependence of the sensor output was assumed to be proportional to a cosine: figure 16 of the data sheet [23] seems to confirm this assumption. In figure 3.1c, the data from figure 16 of the data sheet was fitted to a cosine curve. As one can see this fit is good: the main source of error seems to be the thickness of the line used in the original plot, and the fit only significantly deviates from the data at the edges of the domain: these values are in general not important to the measurements done in the project, since their sensor output will always be small.

The twelve sensors used on the prototype are all connected to a central PCB which relays their measurements to a computer through a USB connection. This central PCB contains a time unit and a heating element, amongst other electronic parts (see figure 3.1a). In order for their measurements to be useful, we needed to know the intensity dependence of the output of the sensors. If one would find a function that relates the light intensity to the sensor output, one could use the inverse of this function to find the intensity corresponding to a certain output, which is what we need in this project. Other variables, such as the comparison of the temperature output between the sensors and the dependence of the light measurement on the temperature would have also been interesting, but due to a lack of time these could not be studied.

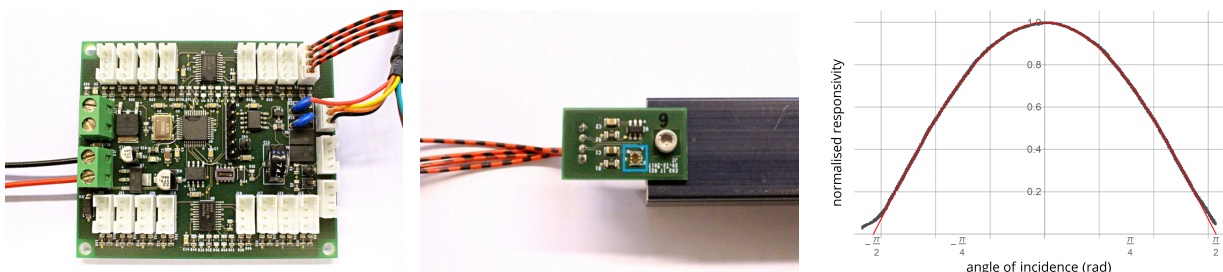


Figure 3.1: a) The central PCB. The red and black cables on the left connect to the power supply, the red-black dotted cables in the top right corner connect to the sensor, and the multi coloured cables on the right connect to the computer. b) Sensor number 9. The light sensor is circled in blue, the red-black dotted cables connect to the central PCB. c) Graph of the data from figure 16 of [23] (black) and a cosine curve fitted to the data (red).

Instrument		Data sheet
Solar simulator	Newport Oriel Sol2A model 94062A	[25, 26]
Power supply solar simulator	Newport model 69920	[27]
Reference cell	Newport Oriel PV reference cell system model 91150V	[24]
Power supply PCB	TTi model EB2025T	[28]

Table 3.1: A summary of the equipment used in this study. The sensors and central PCB were produced by the AMOLF electronic itself. The data sheets can be found in the additional materials.

3.1 Set-up

In the experiment, we used the equipment described in table 3.1. As schematically represented in figure 3.2, we placed the sensor on a moveable platform, which also housed a reference cell. We connected the sensor to the central PCB, which we in turn connected to a power supply at 5 V and to a laptop which read out the sensor values. Jan Zomerdiijk (AMOLF electronics department) wrote the software of the sensors and PCB. We used the open-source Tera Term computer programme to read out the sensor data on the laptop. The reference cell was connected to a monitor that displayed the intensity as measured by the cell in suns¹. The moveable platform could slide the reference cell and the sensor under the solar simulator, thus exposing it to its light. The solar simulator was connected to a variable power supply.

3.2 Methodology

Before the experiment, each sensor was thoroughly cleaned using a cotton bud soaked in ethanol, in order to remove any contamination that might block the light sensor. After this, the sensors were visually inspected using a microscope to look for any remaining contamination; figure 3.3 shows the difference between a clean and a contaminated light sensor. Next, the solar simulator was prepared by setting it to the required power and letting it warm up for about half an hour. The starting power output was 400 W which was increased in steps of 10 W to 500 W during the experiment. It was thought that 400 W was the

¹In what follows, depending on the context a "one-sun" exposure is taken to have a 1000 Wm^{-2} intensity and/or an AM1.5 spectrum [24, 25].

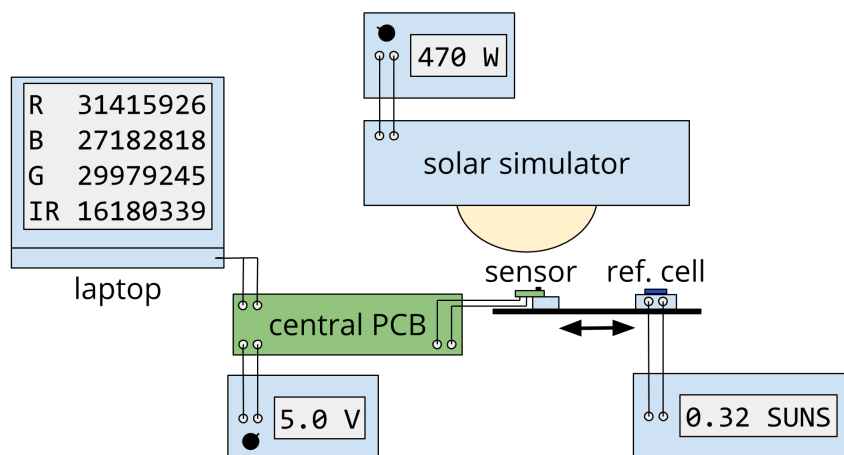


Figure 3.2: A schematic drawing of the experimental set up used in this experiment.



Figure 3.3: a) Optical microscope image of a cleaned light sensor. Note the different filters for the different colour channels, and the clear channel in the middle. b) Optical microscope image of an contaminated light sensor, clearly showing a film of dirt on the sensor surface (note that the microscope was focused on this film; hence the sensor itself is slightly blurry).

minimum power output of the solar simulator², the upper limit was chosen because the red channel of the sensors can only measure intensities up to about 500 W^3 .

Because the power output does only weakly relate to how it simulates the sun (a 1000 W power supply should approximate a one-sun exposure although in practice it was found to be less, see appendix B) a standardised reference cell was used to determine the output of the solar simulator as a fraction of a one-sun exposure. Since the light fluctuates slightly [25, 26], an average over about half a minute of measuring was taken as the measurement value. This time was also used to check for fluctuations larger than a few percent in the reference cell value: larger fluctuations indicate that the solar simulator had not fully warmed up yet.

After this was done, the sensor that we wanted to measure was placed at a fixed position under the solar simulator. It was connected to the central PCB, which was connected to a power supply and to a laptop through a USB cable, as described in the previous section. The sensor was switched on and exposed to the light of the solar simulator for about thirty second, in order for the sensor output to stabilise. After this, the sensor was switched off and its last four measurements of the red, green, blue, and infrared channel were recorded. The average value of these four measurements for each channel was taken to be the measurement of the light intensity. This was then repeated for every sensor.

After measuring all sensors for a certain power input for the solar simulator, the power was increased by 10 W. The light was given about ten to fifteen minutes to warm up again and then the reference cell was used to measure its output. Next all sensors were measured and the cycle would repeat itself, until the power input of the solar simulator reached 500 W. After all sensors had been measured for all eleven intensities, they were once again inspected with an optical microscope for any signs of contamination.

3.3 Results and discussion

The intensity dependence of sensors 2, 3, 7, 14, and 20 are shown in figure 3.4, the linear fits for the data for each colour channel are given in table 3.2. As can be seen, these fits have very high R^2 values and low estimated variances, and through table 3.3 it can be seen that their residuals seem to be randomly distributed: therefore we can conclude that the linear functions given in table 3.2 fit the data well.

As can be seen in table 3.2, the gradient of the fits for each colour do not vary much between sensors and therefore the average gradient can be used in calculations without significantly reducing accuracy. The

²The solar simulator can actually be set to 350 W [27], this was not known when the experiment was done. Even lower exposures of the sensors could be achieved by using ND-filters.

³The clear channel can only measure intensities $< 400 \text{ W}$ and was thus not included in this experiment.

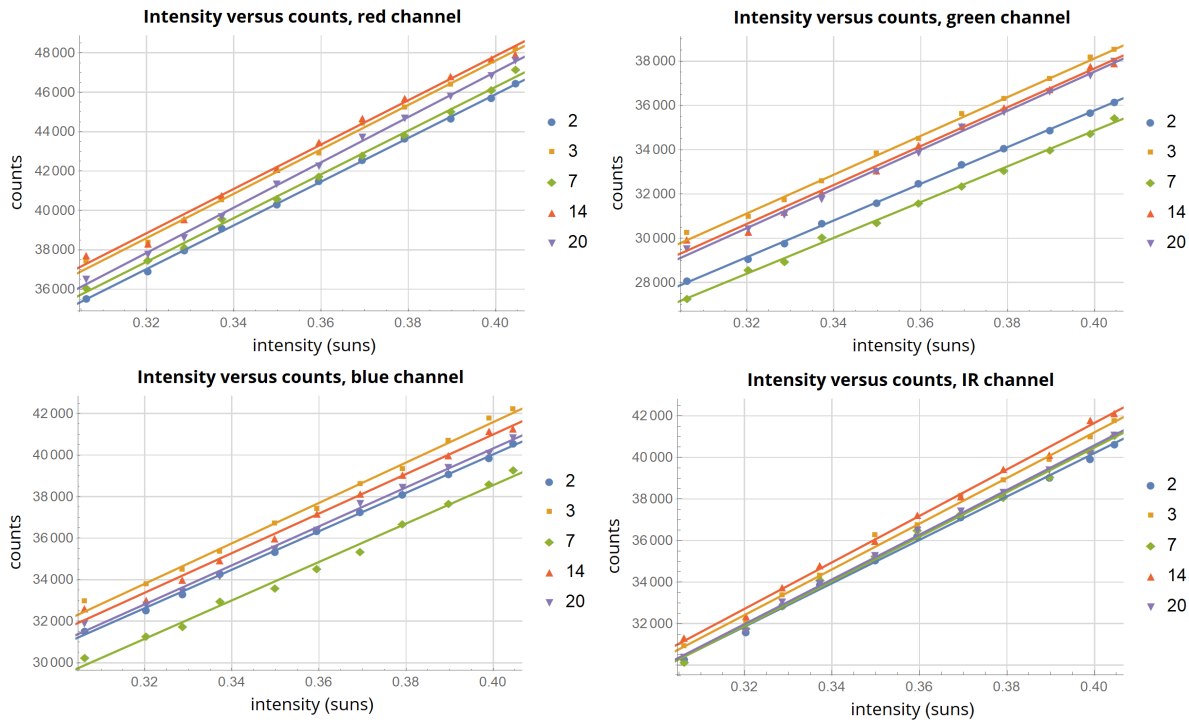


Figure 3.4: Plots of the data obtained in the experiment, for each channel. Included in the graphs are the fits as given in table 3.2.

offset in contrast does vary considerably between sensors. Therefore the sensors of the measurement tool would need to be calibrated in order to produce usable results. However, since only their offset has to be known, a simple calibration would suffice. We propose that before being used, each sensor should be illuminated using a light source with a known power output and a known colour (for instance, red-/green/blue/IR LED's). By using the sensor output and the average gradient discussed above, the offset of the sensor can then be determined. This would be a simple, one-time procedure that would significantly increase the accuracy of the instrument.

Due to the limited number of sensors measured per intensity, any possible time evolution of the intensity of the solar simulator could not be investigated. The data sheet of the solar simulator [25, 26] states that the output of the lamp should be constant, however if the lamp had not completely warmed up (or cooled down, when reducing the power output) before the experiment was started, or due to the lifespan of the lamp, the output might have changed over the course of the experiment. Because this experiment consists only of five sensors it is difficult to determine any time evolution. Nevertheless, the waiting time of at least ten minutes in between measuring the sensors at different power outputs should in general be enough. This could be verified experimentally in a future experiment.

The data given in this chapter is for five sensors only (2, 3, 7, 14, 20). The experiment was repeated using seven more sensors (to wit: 4, 6, 9, 11, 17, 19, 21) in order to have enough characterised sensors for the prototype. Due to a lack of time the data obtained from these sensors could not be incorporated into this report, but it can be found in the additional materials for future use.

In the prototype, the sensor output can be used to determine the illumination (in units of sun) by using the inverse of the fits given in the previous section. For a sensor that is not yet calibrated, the illumination can be approximated using the average gain and the offset acquired through the calibration described in the previous section. For a given colour, one can use the following equation:

$$I = \frac{\text{sensor count} - \text{sensor offset}}{\text{average gradient}}$$

where I is the intensity, in suns, as measured by the sensor.

Sensor #	Colour	Linear fit	R^2	Estimated variance
2	Red	$1532.10 + 110924x$	0.999996	8760.41
	Green	$2652.76 + 82808.4x$	0.999996	5376.43
	Blue	$3031.77 + 92511.7x$	0.999994	10011.8
	IR	$-1536.69 + 104364x$	0.999979	33513.0
3	Red	$2554.51 + 112638x$	0.999984	36871.0
	Green	$3126.30 + 87497.2x$	0.999983	25197.7
	Blue	$2684.91 + 97262.7x$	0.999966	58691.1
	IR	$-2744.00 + 109884x$	0.999962	62835.2
7	Red	$1884.26 + 110978x$	0.999981	39967.8
	Green	$2580.96 + 80713.7x$	0.999983	20345.2
	Blue	$1576.56 + 92445.6x$	0.999949	75258.1
	IR	$-2420.50 + 107239x$	0.999963	59436.1
14	Red	$2841.15 + 112521x$	0.999956	101345
	Green	$2579.65 + 87734.9x$	0.999956	62992.1
	Blue	$2905.12 + 95227.4x$	0.999956	73515.6
	IR	$-3055.04 + 111788x$	0.999971	49463.0
20	Red	$1058.60 + 114968x$	0.999989	101345
	Green	$2210.00 + 88296.5x$	0.999984	62992.1
	Blue	$2809.77 + 93783.7x$	0.999975	73515.6
	IR	$-2428.54 + 107538x$	0.999976	49463.0
Average	Red	$1974.12 + 112406x$		
	Green	$2629.93 + 86352.3x$		
	Blue	$2601.63 + 94246.2x$		
	IR	$-2436.95 + 108162x$		

Table 3.2: Fits for the data generated in the experiment, and their respective R^2 and estimated variance values. The residual plots of these fits can be found in table 3.3. When the intensity in suns is inserted for x , the equations give the number of counts of the sensors.

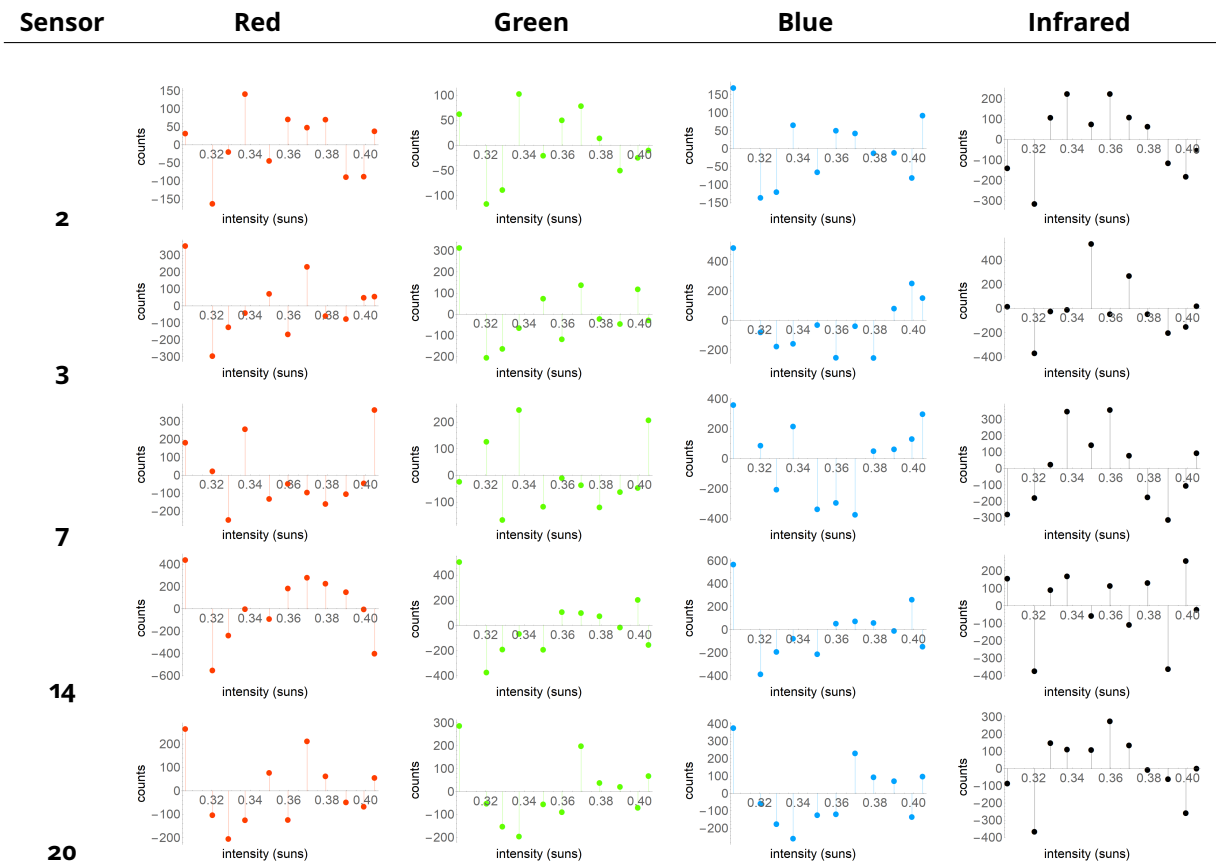


Table 3.3: Residual plots of the fits of table 3.2

Chapter 4

Conclusion and discussion

In the previous chapters, we have shown that the cubical measurement tool developed at AMOLF can be improved by increasing the number of sensor to twelve, which transforms the instrument from a cube into a dodecahedron. Shading on the instrument, due to a ring that holds two half spheres enclosing the instrument together, will decrease the accuracy of the diffuseness metric measurements made by the instrument, but the improved tool will still be more accurate than the original cubical tool, according to our simulations. Furthermore we found that there is no need to fully characterise the sensors that will be used on the instrument: instead, a simple calibration of the offset will suffice to obtain reliable measurements of the light intensity.

The next step in this project is to test the prototype which, at the time of writing, is being built at AMOLF. Only testing can reveal whether the simulations described chapter 2 were valid. The simplest manner of doing this would be to compare the output of the measurement tool to existing diffuseness measurement tools, as was done in a previous project [5]. By comparing the diffuseness calculated by both tools and the simulation results given in this report, the conclusions of the simulations can be tested experimentally.

In chapter 3 we mentioned that we did not characterise the dependence of the sensor output on temperature. This might pose a problem because the instrument will subject to high temperatures due to the intensity of incoming solar radiation, especially in summer, since it is a small black tool enclosed in a transparent sphere. This might affect the measurements, and therefore it would be wise to characterise the temperature dependence of the sensors before the instrument is exposed to intense solar radiation. Lower temperatures, and the condensation and freezing of water associated with them, will not be an issue due to the heating element included in the instrument.

We are still left with some unanswered questions about both the model and the tool. One of them is whether we could correct the error due to direct light shading. Since direct light comes from the sun¹, and since we can both calculate which positions of the sun cause shading (through the simulation given in chapter 2) and the position of the sun at any given moment, we should be able to predict in which cases the diffuseness measurements will be corrupted by shading. Through the simulation, we can calculate what the diffuseness metric would have been without shading, and thus we could correct these measurements. This does require that the model be improved further: the exact orientation of the instrument and the environment in which it is placed have to be taken into account. This way, it should at least be feasible to correct for some of the erroneous diffuseness values due to shading of the direct light field by the ring.

Future projects could also look into other uses of the instrument. For instance, since the instrument measures various colour channels, the intensities measured could perhaps be used to reconstruct the

¹Incidentally, direct lighting will result from specular reflection such as windows are cars driving by. We disregard these occurrences here since they will be responsible for only a tiny fraction of the total direct light shading errors.

spectrum of incoming solar radiation. This could be done by using comparing the intensities to known solar spectra and fitting the data to (a combination of) those spectra. As mentioned in section 1.1, the solar spectrum is an important factor affecting solar cell performance, therefore making it interesting to have a tool that can study both diffuseness and spectrum. Furthermore, since each face measures the intensity of incoming solar radiation, the effect of the various combination of light intensities (using both their magnitude and spatial location, rather than just their overall magnitude as with the diffuseness metric) can also be studied. This is less relevant, because in general the highest intensity of light will originate from the sun (the position of which is known), but it might reveal the occurrence of specular reflections from the environment, for instance.

Bibliography


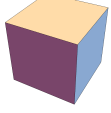
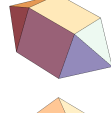


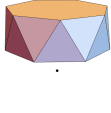
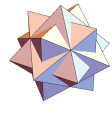
1. Evershed, N. *Carbon countdown clock: how much of the world's carbon budget have we spent?* 2017. <https://www.theguardian.com/environment/datablog/2017/jan/19/carbon-countdown-clock-how-much-of-the-worlds-carbon-budget-have-we-spent> (2018).
2. IPCC. *Climate change 2014: synthesis report. contribution of working groups I, II and III to the fifth assessment report of the intergovernmental panel on climate change*. 2–26. ISBN: 9789291691432. doi:10.1017/CBO9781107415324. arXiv: arXiv:1011.1669v3 (IPCC, Geneva, 2014).
3. IPCC. *Climate change 2014: mitigation of climate change* 1454. ISBN: 9781107654815. doi:10.1017/CBO9781107415416. arXiv: arXiv:1011.1669v3. <http://www.ipcc.ch/report/ar5/wg3/> (2014).
4. Velds, C. *Zonnestraling in Nederland [Dutch]*. 170. ISBN: 905210140X (De Bilt, 1993).
5. Maassen, T. *The effect of light diffuseness on the outdoor performance of thin film solar cells*. Bachelor thesis (University of Amsterdam, 2017).
6. Cuttle, C. Lighting patterns and the flow of light. *Lighting Research & Technology* **3**, 171–189. ISSN: 14771535 (1971).
7. Xia, L., Pont, S. C. & Heynderickx, I. Light diffuseness metric: part 1 theory. *Lighting Research and Technology* **49**, 411–427. ISSN: 14771535 (2017).
8. NREL. *Device Performance: measurements and characterization* <https://www.nrel.gov/docs/fyo6osti/40123.pdf> (Golden, 2009).
9. Nelson, J. *The physics of solar cells*. 1st ed. ISBN: 139781860943409 (Imperial College Press, London, 2003).
10. Shah, A. in *Practical handbook of photovoltaics: Fundamentals and applications* (eds McEvoy, A., Markvart, T & Castañer, L.) 2nd ed., 259–281 (Academic Press, 2012). ISBN: 978-0-12-385934-1.
11. Polo, J., Alonso-Abella, M., Ruiz-Arias, J. A. & Balenzategui, J. L. Worldwide analysis of spectral factors for seven photovoltaic technologies. *Solar Energy* **142**, 194–203. ISSN: 0038092X (2017).
12. Ishii, T., Otani, K., Takashima, T. & Xue, Y. Solar spectral influence on the performance of photovoltaic modules under fine weather and cloudy weather conditions. *Progress in Photovoltaics: Research and Applications* **21**, 481–489 (2013).
13. Nofuentes, G., de la Casa, J., Solís-Alemán, E. M. & Fernández, E. F. Spectral impact on PV performance in mid-latitude sunny inland sites: Experimental vs. modelled results. *Energy* **141**, 1857–1868. ISSN: 03605442 (2017).
14. Eke, R., Betts, T. R. & Gottschalg, R. Spectral irradiance effects on the outdoor performance of photovoltaic modules. *Renewable and Sustainable Energy Reviews* **69**, 429–434. ISSN: 18790690 (2017).
15. Oxford English Dictionary. *Albedo*. 2018. <https://en.oxforddictionaries.com/definition/albedo>.
16. Sun, X., Khan, M. R., Deline, C. & Alam, M. A. Optimization and performance of bifacial solar modules: A global perspective. *Applied Energy* **212**, 1601–1610. ISSN: 03062619 (2018).



17. Jager, K, Isabelle, O, Smeth, A & Zeman, M. *Solar energy: fundamentals, technology, and systems*. (Delft University of Technology, Delft, 2014).
18. Ineichen, P. & Perez, R. A new airmass independent formulation for the Linke turbidity coefficient. *Solar Energy* **73**, 151–157. ISSN: 0038092X (2002).
19. Nave, R. *Blue sky*. <http://hyperphysics.phy-astr.gsu.edu/hbase/atmos/blusky.html> (2018).
20. Cuttle, C. Research note: a practical approach to cubic illuminance measurement. *Lighting Research and Technology* **46**, 31–34. ISSN: 14771535 (2014).
21. Weisstein, E. W. *Thomson problem*. <http://mathworld.wolfram.com/ThomsonProblem.html> (2018).
22. Xia, L., Pont, S. C. & Heynderickx, I. Light diffuseness metric, Part 2: Describing, measuring and visualising the light flow and diffuseness in three-dimensional spaces. *Lighting Research and Technology* **49**, 428–445. ISSN: 14771535 (2017).
23. *TCS3400 color light-to-digital converter datasheet*. 1–34 (ams AG, Premstaetten, 2016).
24. *Model 9150V user's manual*. 1–14 (Newport corporation, Bozeman, 2018).
25. *Oriel Sol2A*. 1–4 (Newport corporation, Irvine, 2018).
26. *9200XF solar simulator field recertification service*. 1–2 (Newport corporation, Irvine).
27. *Arc lamp power supply, universal, 350 to 1200 Watt*. 2018. <https://www.newport.com/p/69920> (2018).
28. *Shortform catalogue: laboratory DC power supplies*. **3** (Thurlby Thandar Instrumens limited, Huntingdon, 2010).
29. Weisstein, E. W. *Spherical coordinates*. <http://mathworld.wolfram.com/SphericalCoordinates.html> (2018).

Appendix A

Polyhedrons

The vertices of the following polyhedrons were used as the coordinates of the points for the following number of points:

Points	Polyhedron	
6	Octahedron	
8	Cube	
10	Elongated square dipyramid	
12	Icosahedron	
14	Cumulated cube	
16	Unit equilateral heptagonal antiprism with added top $((0, 0, 1))$ and bottom $((0, 0, -1))$ points	
18	Octahedron three compound	

Points	Polyhedron	
20	Dodecahedron	
22	Rhombic icosahedron	
24	Small rhombicuboctahedron	
26	Disdyakis dodecahedron	

Appendix B

Solar simulator versus reference cell

As mentioned in chapter 3, the power output of the solar simulator (as measured by the reference cell) does not match the power output as dictated by the power supply of the solar simulator. Instead, it is significantly lower as can be seen in the figure below (where "sun" refers to a 1,000 W output). Note that the intensity as measured by the reference cell depends on where it is placed under the solar light. However, for the experiment described in chapter 3, the sensor output of difference output under equal intensities mattered, not the exact intensity itself.

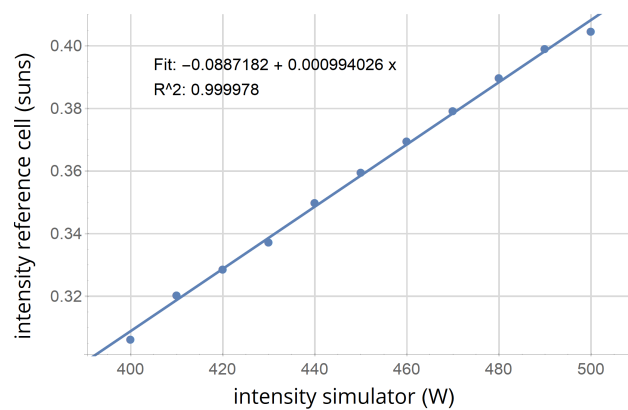


Figure B.1: Comparison of the input power to the solar simulator and the output as measured by the reference cell.

Appendix C

Code

Listed below is the code discussed in this document. Some of the functions and calculations listed below (most notably, `figureofmeritdata` and `comparisondata`) can take several minutes to several hours to run: the data they generate can therefore be exported and imported so that the functions do not have to be run again and again. In order to use the importing and exporting functions, the path of the files has inserted in the `Import[]` functions. The various files can be found in the additional materials.

Note that the code is not made to be fool-proof: one can for instance use strings or images as input for the metric calculations, which will either result in errors or in falsely calculated values. Thus, when using the code, always ensure that returned values are calculated with physically sound variables as input.

On a technical note, this document uses the convention for spherical coordinates laid out in figure 2. These are different from Mathematica's definition of spherical coordinates, therefore the code uses custom functions for transformations from Cartesian to spherical coordinates (`tospherical[]`) and vice versa (`tocartesian[]`). To this end, Mathematica's `arctan(y/x)`-function is used (`ArcTan[x,y]`) which takes into account which quadrant the point (x,y) is in. The following transformations are used for $(x,y,z) \mapsto (r,\theta,\phi)$ and back [29]:

$$\begin{bmatrix} x \\ y \\ z \end{bmatrix} \mapsto \begin{bmatrix} r \cos \theta \sin \phi \\ r \sin \theta \sin \phi \\ r \cos \phi \end{bmatrix} \quad \begin{bmatrix} r \\ \theta \\ \phi \end{bmatrix} \mapsto \begin{bmatrix} \sqrt{x^2 + y^2 + z^2} \\ \arctan\left(\frac{y}{x}\right) \\ \arccos\left(\frac{z}{r}\right) \end{bmatrix} \quad (\text{C.1})$$

```
(* Simulation measurement tool, 30 May 2018
Code tested and approved for Mathematica 11.2 and 11.3 *)

(* =====
1. Preamble
===== *)

Remove["Global'*" ]
tospherical[{xx_, yy_, zz_}] := {Sqrt[xx^2 + yy^2 + zz^2], ArcTan[yy/xx],
ArcCos[zz/Sqrt[xx^2 + yy^2 + zz^2]]}
tocartesian[{r_, \[Theta]_, \[Phi]_}] := {r*Cos[\[Theta]]*Sin[\[Phi]], r*Sin[\[Theta]]*Sin[\[Phi]], r*Cos[\[Phi]]}

(* =====
2. Choosing number of measurement points
===== *)

(* 2.1 Import *)
```

```

figureofmeritdata = Flatten[Import["PATH//FigureOfMeritData.csv", "Data"];
comparisondata = Import["PATH//ComparisonData.mx", "Table"];

comparisondatapart[j_]:= Import[StringJoin["PATH\\comparisondata_",
ToString[j], ".csv"], "Data"]

(* 2.2 Figure of merit *)

figureofmerit[fraction_, coordinates_] := Module[{},
  Which[coordinates[[3]] < 0, coordinates[[3]] = Abs[coordinates[[3]]];

  direct := (1 - fraction)*Normalize[coordinates];

  diffuse[a_, b_, c_] := fraction*Normalize[{a, b, c}];

  illuminance[d_, e_, f_] := If[Dot[diffuse[d, e, f], Normalize[{d, e, f}]] >= 0,
    Dot[diffuse[d, e, f], Normalize[{d, e, f}]], 0] +
    If[Dot[direct, Normalize[{d, e, f}]] >= 0, Dot[direct, Normalize[{d, e, f}]], 0];

  figure = 0.5*NIntegrate[Abs[illuminance[d, e, f] - illuminance[-d, -e, -f]],
    {d, e, f} \[Element] Ball[{0, 0, 0}, 1]]/
    NIntegrate[illuminance[d, e, f], {d, e, f} \[Element] Ball[{0, 0, 0}, 1]]

fractionvalues = {0,0.1,0.2,0.3,0.4,0.5,0.6,0.7,0.8,0.9,1};

figureofmeritdata = Table[figureofmerit[l,{1,1,1}/Sqrt[3]],{l,fractionvalues}];

figureofmeritassociation = Association[Table[fractionvalues[[j]]->figureofmeritdata[[j]],{j,1,11}];

Export["PATH//FigureOfMeritData.csv", figureofmeritdata]

(* 2.3 Metric *)

metric[points_, fraction_, coordinates_] := Module[{},
  Which[coordinates[[3]] < 0, coordinates[[3]] = Abs[coordinates[[3]]];

  direct := (1 - fraction)*Normalize[coordinates];
  diffuse[{a_, b_, c_}] := fraction*Normalize[{a, b, c}];

  Which[points == 6, normals = Normalize[#] & /@ PolyhedronData["Octahedron", "Vertices"],
    points == 8, normals = Normalize[#] & /@ PolyhedronData["Cube", "Vertices"],
    points == 10, normals = Normalize[#] & /@ PolyhedronData["ElongatedSquareDipyramid", "Vertices"],
    points == 12, normals = Normalize[#] & /@ PolyhedronData["Icosahedron", "Vertices"],
    points == 14, normals = Normalize[#] & /@ PolyhedronData["CumulatedCube", "Vertices"],
    points == 16, normals = Append[Append[Normalize[#] & /@ PolyhedronData[{"Antiprism", 7}, "Vertices"],
    {0, 0, 1}], {0, 0, -1}],
    points == 18, normals = Normalize[#] & /@ PolyhedronData["OctahedronThreeCompound", "Vertices"],
    points == 20, normals = Normalize[#] & /@ PolyhedronData["Dodecahedron", "Vertices"],
    points == 22, normals = Normalize[#] & /@ PolyhedronData["RhombicIcosahedron", "Vertices"],
    points == 24, normals = Normalize[#] & /@ PolyhedronData["SmallRhombicuboctahedron", "Vertices"],
    points == 26, normals = Normalize[#] & /@ PolyhedronData["DisdyakisDodecahedron", "Vertices"]
  ];

  illuminance[d_] := If[ Dot[diffuse[d], Normalize[d]] >= 0, Dot[diffuse[d], Normalize[d]], 0] +
    If[ Dot[direct, Normalize[d]] >= 0, Dot[direct, Normalize[d]], 0];

  vector[e_] := Abs[illuminance[e] - illuminance[-e]];

  metriccalculation = 0.5*Sum[vector[f], {f, normals}]/Sum[illuminance[g], {g, normals}]
]

(* 2.4 Comparison figure of merit and metric *)

comparisondata = Table[Abs[metric[k, l, RandomPoint[Sphere[]]] - figureofmeritassociation[l]]/
  figureofmeritassociation[l],5000, {l, {0, 0.1, 0.2, 0.3, 0.4, 0.5, 0.6, 0.7, 0.8, 0.9, 1}},
  {k, {6, 8, 10, 12, 14, 16, 18, 20, 22, 24, 26}}];

```

```

comparisonmean = Table[Mean[Table[comparisondata[[k, j, i]], {k, 1, 5000}], {i, 1, 11}, {j, 1, 11}];

comparisondatapart[j_]:=comparisondata[[All, All, j]]

Export[StringJoin["PATH\\comparisondata_",
  ToString[#], ".csv"], comparisondatapart[#]&/@Range[1, 11]

(* =====
3. Implementing shadow for n = 12
===== *)

(* 3.1 Import *)

comparisontwelweshadowdata = Import["PATH//ComparisonTwelveData.csv", "Data"];

(* 3.2 Metric for twelve points with shadow *)

metrictwelvepointswithshadow[fraction_, coordinates_] := Module[{},
  direct := (1 - fraction)*Normalize[coordinates];

  diffuse[{a_, b_, c_}] := fraction*Normalize[{a, b, c}];

  shadediffuse[h_] := If[Dot[diffuse[h], Normalize[h]] >= 0, If[h != {0, 0, 1} && h != {0, 0, -1},
    0.974, 1], 0];

  shadirect[i_, j_] := Module[{},
    pointtorim := tocartesian[{1, tospherical[i][[2]],
      tospherical[tocartesian[{3, tospherical[i][[2]], Pi/2}] - j][[3]]}];
    shadecalculation = If[Dot[Normalize[i], j] > 0 && Abs[Dot[Normalize[i], pointtorim]] < 0.9983, 1, 0];
    returns = If[NumericQ[shadecalculation], shadecalculation, 0];

normals = {
  {0, 0, 1}, {0, 0, -1}, {0.2766, -0.8505, 0.4473}, {-0.2766, 0.8505, -0.4473}, {0.8944, 0, 0.4472},
  {-0.8944, 0, -0.4472}, {0.2766, 0.8505, 0.4473}, {-0.2766, -0.8505, -0.4473}, {-0.7238, 0.5254, 0.4472},
  {0.7238, -0.5254, -0.4472}, {-0.7238, -0.5254, 0.4472}, {0.7238, 0.5254, -0.4472}};

  illuminance[d_] := Dot[diffuse[d], Normalize[d]]*shadediffuse[d] + Dot[direct,
    Normalize[d]]*shadirect[Normalize[coordinates], d];

  vector[e_] := Abs[illuminance[e] - illuminance[-e]];

  metriccalculation = 0.5*Sum[vector[f], {f, normals}]/Sum[illuminance[g], {g, normals}]

(* 3.3 Comparison metric and figure of merit *)

comparisontwelweshadowdata = Table[Table[ Abs[metrictwelvepointswithshadow[l, RandomPoint[Sphere[]]] -
  figureofmeritassociation[l]]/figureofmeritassociation[l], 10000],
  {l, {0, 0.1, 0.2, 0.3, 0.4, 0.5, 0.6, 0.7, 0.8, 0.9, 1}}];

Export["PATH//ComparisonTwelveData.csv", comparisontwelweshadowdata]

```